

# Estimating the relevance of predictions from nuclear mean-field models

P.-G. Reinhard\*

Institut für Theoretische Physik II, Universität Erlangen-Nürnberg,  
Staudtstrasse 7, D-91058 Erlangen, German

PACS REF: 02.60.Pn, 02.70.Rr, 21.10.Dr, 21.10.Ft, 21.60.Jz, 21.65.Ef, 24.30.Cz

September 22, 2015

## Abstract

This contribution reviews the present status of the Skyrme-Hartree-Fock (SHF) approach as one of the leading self-consistent mean-field models in the physics of atomic nuclei. It starts with a brief summary of the formalism and strategy for proper calibration of the SHF functional. The main emphasis lies on an exploration of the reliability of predictions, particularly in the regime of extrapolations. Various strategies are discussed to explore the statistical and systematic errors of SHF. The strategies are illustrated on examples from actual applications. Variations of model and fit data are used to get an idea about systematic errors. The statistical error is evaluated in straightforward manner by statistical analysis based on  $\chi^2$  fits. This also allows also to evaluate the correlations (covariances) between observables which provides useful insights into the structure of the model and of the fitting strategy.

## 1. Introduction

This contribution is devoted to a brief review of the Skyrme-Hartree-Fock (SHF) approach to nuclear structure and dynamics with emphasis on a critical analysis of its predictive power. SHF belongs to the class of nuclear self-consistent mean-field models which became competitive in the early 1970ies. The first nuclear models were purely macroscopic of the type of a liquid drop model. The observation of shell structure led to the invention of an empirical mean-field model, the nuclear shell model, with which one could reveal the basic mechanisms of nuclear structure from magic nuclei over deformation to low-energy collective motion for overviews see the much celebrated nobel lectures [1, 2, 3] and books [4]. These findings have confirmed that nuclear structure and dynamics can be well described in terms of a mean-field. The mixed macroscopic-microscopic model employing empirical shell models has been driven to a precise instrument of describing and predicting nuclear masses, see e.g. [5]. Parallel to these developments, one has looked for the natural next step, namely for self-consistent mean-field models of the type of the Hartree-Fock approximation. Self consistency eliminates the need for intuitive explicit shaping of the mean-field potential and is thus applicable to a much broader range of processes.

The SHF approach resembles Hartree-Fock but uses an effective interaction, called the Skyrme force. In fact, it is more precise to say that it uses an effective energy func-

tional derived from the Skyrme force. The Skyrme force was proposed already in [6], had a break-through for practical applications with the first high-quality parametrizations coming up [7], and has evolved meanwhile to one of the most widely used standard schemes for self-consistent nuclear modeling. There are many more models of that sort which rely on effective energy functionals. The two strongest competitors of SHF are the Gogny force [8, 9] and the relativistic mean-field (RMF) model [10, 11] for which meanwhile a couple of variants exists [12]. For a review of all three nuclear effective energy functionals see [13]. It is interesting to note that these nuclear effective energy functionals became fashionable almost at the same time as density functional theory for electronic systems [14, 15, 16]. The difference is that electronic energy functionals have been derived from first principle and ab-initio calculations while nuclear functionals are mostly determined by calibration with respect to empirical data. That is because the nuclear many-body problem is by orders of magnitude more involved than that for electrons. In spite of considerable progress in nuclear ab-initio calculations (for reviews see e.g. [17, 18, 19, 20, 21]), the case is still not sufficiently well settled to serve as basis for high-quality functionals. The standard pathway is since the early days to motivate the form of the functional by the basic structure of a low-momentum expansion and to calibrate the parameters of the functional by fits to empirical data, usually nuclear ground state properties. This raises the problem how to get an idea about the predictive power of the effective energy functional and to estimate the uncertainties in extrapolations to observables outside the pool of fit data. As we know, it holds for every physical theory that it can never be ultimately proven, but only be confirmed stepwise by experience until one hits the range of validity. This holds even more true for nuclear mean-field models in their pragmatic mix of theoretical and empirical input. It is the main topic of this contribution to present and discuss the various approaches to estimating the uncertainties within nuclear self-consistent mean-field models. Thereby we confine the considerations to the SHF functional as a prototype example. The results are transferable to the competitors, the Gogny force and the RMF.

The paper is outlined as follows: Section 2 summarizes the SHF functional as it is used throughout the paper and sketches its formal motivation. Section 3 briefly collects the various observables employed for calibration of

\*e-mail: paul-gerhard.reinhard@fau.de

the SHF functional (bulk properties of the ground states of finite nuclei), for characterization (response properties of homogeneous nuclear matter), and in a broad range of further applications. Section 4 introduces the method of least-squares ( $\chi^2$ ) fits and the subsequent statistical analysis delivering extrapolation uncertainties and correlations (also coined covariances) between observables. Section 5 addresses the problem of error estimates from many different perspectives. Section 6 exemplifies most of the methods compiled in section 5 in terms of practical applications to a variety of different observables.

## 2. The SHF energy-density functional

### 2.1. Basic constituents: Densities and currents

Mean-field theories describe a system through a set of single particle (s.p.) wavefunctions  $\varphi_\alpha(\mathbf{r})$  and associated BCS amplitudes  $v_\alpha$  for occupation and the complementing  $u_\alpha = \sqrt{1 - v_\alpha^2}$  for non-occupation. These are summarized in the one-body density matrix

$$\varrho_q(\mathbf{r}, \mathbf{r}') = \sum_{\alpha \in q} w_\alpha v_\alpha^2 \varphi_\alpha(\mathbf{r}) \varphi_\alpha^\dagger(\mathbf{r}') \quad (1)$$

where  $q$  labels the nucleon species with  $q = p$  for protons and  $q = n$  for neutrons. The  $w_\alpha$  is a further factor which serves to terminate the summations, so to say a cutoff for pairing space. It will be discussed in connection with the pairing functional in section 2.2.3.

The Skyrme-Hartree-Fock (SHF) energy-density functional requires the knowledge of only a few local densities and and currents. These are, sorted according to time parity:

time even:

$$\begin{aligned} \rho_q &= \text{tr}_\sigma \{ \varrho(\mathbf{r}, \mathbf{r}') \} \big|_{r=r'} && \equiv \text{density} \\ \tau_q &= \text{tr}_\sigma \{ \nabla_r \nabla_{r'} \varrho(\mathbf{r}, \mathbf{r}') \} \big|_{r=r'} && \equiv \text{kinetic density} \\ \mathbf{J}_q &= -i \text{tr}_\sigma \{ \nabla_r \times \hat{\boldsymbol{\sigma}} \varrho(\mathbf{r}, \mathbf{r}') \} \big|_{r=r'} && \equiv \text{spin-orbit density} \end{aligned}$$

time odd:

$$\begin{aligned} \sigma_q &= \text{tr}_\sigma \{ \hat{\boldsymbol{\sigma}} \varrho(\mathbf{r}, \mathbf{r}') \} \big|_{r=r'} && \equiv \text{spin density} \\ \mathbf{j}_q &= \Im m \{ \text{tr}_\sigma \{ \nabla_r \varrho(\mathbf{r}, \mathbf{r}') \} \} \big|_{r=r'} && \equiv \text{current} \\ \boldsymbol{\tau}_q &= -\text{tr}_\sigma \{ \hat{\boldsymbol{\sigma}} \nabla_r \nabla_{r'} \varrho(\mathbf{r}, \mathbf{r}') \} \big|_{r=r'} && \equiv \text{kinetic spin-dens.} \end{aligned}$$

time mixed:

$$\xi_q = \sum_{\alpha \in q} w_\alpha u_\alpha v_\alpha |\varphi_\alpha|^2 \quad \equiv \text{pairing density} \quad (2)$$

It is advantageous to handle the densities in terms of isospin  $T \in \{0, 1\}$  instead of protons  $p$  and neutrons  $n$ . Thus we will often consider the recoupled forms which read for the local density

$$\rho_0 \equiv \rho = \rho_p + \rho_n \quad , \quad \rho_1 = \rho_p - \rho_n \quad , \quad (3)$$

and similarly for the other densities and currents. The isoscalar density  $\rho_0 \equiv \rho$  is equivalent to the total density and the difference  $\rho_1$  corresponds to the isovector density. All densities and currents in the collection (2) are real and have definite time parity, except for the pairing density  $\xi$  which is complex and has mixed time parity.

Note that the above collection of densities and currents is richer than in electronic density-functional theory (DFT) which employs usually only the local (spin) density  $\rho_\sigma(\mathbf{r})$  [22]. This indicates that nuclear DFT is different [23]. This will also become apparent later on in connection with the calibration of the energy functional, see section 4 which proceeds much different than for electronic DFT.

### 2.2. The composition of the total energy

Starting point of all self-consistent mean-field theories based on DFT is an expression for the total energy. This reads for SHF

$$E_{\text{total}} = \int d^3r \mathcal{E}_{\text{kin}} + \int d^3r \mathcal{E}_{\text{Sk}} + E_{\text{Coul}} + E_{\text{pair}} - E_{\text{corr}} \quad . \quad (4)$$

The one-body kinetic energy is given by

$$\mathcal{E}_{\text{kin}} = \frac{\hbar^2}{2m_p} \tau_p + \frac{\hbar^2}{2m_n} \tau_n \quad . \quad (5)$$

Keeping it at the exact level implies that full quantum mechanical shell structure is maintained which means that we deal with DFT at the level of the Kohn-Sham approach [15, 22].

#### 2.2.1. The Skyrme energy functional

Key piece is the SHF energy density:

$$\mathcal{E}_{\text{Sk}} = \mathcal{E}_{\text{Sk,even}} + \mathcal{E}_{\text{Sk,odd}} \quad , \quad (6a)$$

$$\begin{aligned} \mathcal{E}_{\text{Sk,even}} = & \quad C_0^\rho \rho_0^2 & + & \quad C_1^\rho \rho_1^2 \\ & + C_0^{\rho,\alpha} \rho_0^{2+\alpha} & + & \quad C_1^{\rho,\alpha} \rho_1^2 \rho_0^\alpha \\ & + C_0^{\Delta\rho} \rho_0 \Delta\rho_0 & + & \quad C_1^{\Delta\rho} \rho_1 \Delta\rho_1 \\ & + C_0^{\nabla J} \rho_0 \nabla \cdot \mathbf{J}_0 & + & \quad C_1^{\nabla J} \rho_1 \nabla \cdot \mathbf{J}_1 \\ & + C_0^\tau \rho_0 \tau_0 & + & \quad C_1^\tau \rho_1 \tau_1 \\ & + C_0^J \mathbf{J}_0^2 & + & \quad C_1^J \mathbf{J}_1^2 \end{aligned} \quad (6b)$$

$$\begin{aligned} \mathcal{E}_{\text{Sk,odd}} = & \quad C_0^\sigma \sigma_0^2 & + & \quad C_1^\sigma \sigma_1^2 \\ & + C_0^{\sigma,\alpha} \sigma_0^2 \rho_0^\alpha & + & \quad C_1^{\sigma,\alpha} \sigma_1^2 \rho_0^\alpha \\ & + C_0^{\Delta\sigma} \sigma_0 \Delta\sigma_0 & + & \quad C_1^{\Delta\sigma} \sigma_1 \Delta\sigma_1 \\ & + C_0^{\nabla J} \sigma_0 \cdot \nabla \times \mathbf{j}_0 & + & \quad C_1^{\nabla J} \sigma_1 \cdot \nabla \times \mathbf{j}_1 \\ & - C_0^\tau \mathbf{j}_0^2 & - & \quad C_1^\tau \mathbf{j}_1^2 \\ & - \frac{1}{2} C_0^J \sigma_0 \cdot \boldsymbol{\tau}_0 & - & \quad \frac{1}{2} C_1^J \sigma_1 \cdot \boldsymbol{\tau}_1 \end{aligned} \quad (6c)$$

The formal reasoning for this functional will be presented in section 2.3. But already here, the building principle is obvious: The energy density contains all conceivable bilinear couplings of densities and currents up to second order in derivatives. Each term is time even, although it may be composed of a product of two time-odd currents. The coupling constants are denoted as  $C_T^{\text{type}}$  with obvious abbreviations for “type”. Each coupling constant depends, in principle, on the isoscalar density  $\rho_0$ . In practice, one takes a minimalistic approach and augments only the  $\rho_0^2$  term by a minimalistic density dependence  $\propto C_T^{\rho,\alpha}$ . This suffices to deliver a good description of ground state properties and excitations. On the other hand, more density dependence is hard to determine empirically from nuclear

data because finite nuclei cover a small range of densities due to nuclear saturation.

There is a hierarchy of importance in the various terms of the functional (6). The leading terms are those which depend on  $\rho_T$  only. These already provide a good description of bulk matter and an acceptable, although rough, zeroth order description of nuclei, see section 6.1. Terms with derivatives add details which lift the model to the level of a quantitative description. The minimal set of terms is indicated by yellow (gray) shading. Already these terms alone provide an excellent description of bulk properties of finite nuclei (energy, charge radius, charge surface thickness). All further terms are necessary to allow also a good description of response properties as giant resonances, polarizability, low-energy vibrations, or fission. A large part of the discussions in this manuscript deals with exploring the impact of the various terms on the modeling.

The part  $\mathcal{E}_{\text{Sk,odd}}$  collecting all coupling with time-odd currents is inactive in static calculations, e.g., for ground states of even-even nuclei. They come into play with excitations and with odd nuclei. Note that part of the coefficients, those printed in gray, are taken over from the time-even part. There is no freedom to chose them differently because identity of these coefficients is crucial to guarantee Galilean invariance of the functional [13, 24]. There are choices for the other coefficients. They are all connected with terms carrying spin and become active only for odd nuclei and spin excitations. We will postpone a discussion of these spin terms and their coefficients to section 6.6. All excitation modes in even-even nuclei with natural parity (giant resonances, low-lying vibrational states, rotation) access only the terms in  $\mathcal{E}_{\text{Sk,odd}}$  which are fixed by Galilean invariance.

The functional (6b) contains two terms leading to a spin-orbit potential. The compulsory basic term is the one  $\propto \rho \nabla \cdot \mathbf{J}$ . Its strength  $c_T^{\nabla \cdot \mathbf{J}}$  is an independent parameter of the SHF functional (much unlike relativistic models where the spin-orbit strength is automatically given by the Dirac structure of the wavefunctions [10, 11, 25]). The other term  $\propto \mathbf{J}^2$  is called tensor spin-orbit term. Its parameter  $C_T^J$  is linked to the parameter  $c_T^{\nabla \cdot \mathbf{J}}$  of the kinetic term, see table 3. In fact, we quote here only a simplified version. The full tensor term has true tensor structure (not reduced to a vector  $\mathbf{J}$ ) and there is a complementary tensor term. These tensor terms are ignored in the majority of SHF applications, i.e. one deals with  $c_T^{\nabla \cdot \mathbf{J}} = 0$ . This is what we will assume throughout the following. We refer to [26, 27] for a very detailed survey of tensor terms and its effects in a great variety of observables.

Before continuing with the other contributions to the total energy (4), we mention in passing that the SHF functional (6) does not necessarily guarantee unconditional stability. In particular spin and tensor terms are likely to induce instabilities in symmetry unrestricted calculations. This important issue has been discussed over the years in several respects. For recent extensive studies see, e.g., [26, 27, 28, 29].

### 2.2.2. Coulomb energy

The Coulomb energy is treated as

$$E_{\text{Coul}} = E_{\text{Coul,dir}} - E_{\text{Coul,ex}} \quad , \quad (7a)$$

$$E_{\text{Coul,dir}} = \frac{e^2}{2} \int d^3r d^3r' \frac{\rho_p(\mathbf{r})\rho_p(\mathbf{r}')}{|\mathbf{r} - \mathbf{r}'|} \quad , \quad (7b)$$

$$E_{\text{Coul,ex}} = \frac{3e^2}{4} \left(\frac{3}{\pi}\right)^{1/3} \int d^3r [\rho_p(\mathbf{r})]^{4/3} \quad , \quad (7c)$$

where  $e^2 = 1.44 \text{ MeV fm}$ . Coulomb exchange is done at the level of the local-density approximation [22]. It is to be noted that not all mean-field models include Coulomb exchange (for example, most RMF models do not). In the present examples, it is included. The direct Coulomb energy should employ, in principle, the charge density  $\rho_C$ . However, the mere proton density  $\rho_p$  is used in most applications. This makes not much of a difference and is simpler to handle. We follow this tradition also here.

### 2.2.3. Pairing energy

Pairing is inevitable in case of open shell nuclei. They have a high density of almost degenerated states. This gives the residual two-body interaction a chance to mix these states in order to produce a unique ground state [30]. Pairing explores what is called the particle-particle ( $pp$ ) channel of the effective interaction which is different from the particle-hole ( $ph$ ) channel responsible for the mean field [31]. Thus it is justified and customary to use a separate functional for pairing, namely

$$E_{\text{pair}} = \frac{1}{4} \sum_{q \in \{p,n\}} V_{\text{pair},q} \int d^3r \xi_q^2 \left[ 1 - \frac{\rho_0}{\rho_{0,\text{pair}}} \right] \quad , \quad (8)$$

where  $\rho$  and  $\xi$  are the particle and pairing densities as defined in eq. (2). The pairing functional (8) contains a continuous switch, the parameter  $\rho_{0,\text{pair}}$ , where a pure  $\delta$ -interaction (DI) is recovered for  $\rho_{0,\text{pair}} \rightarrow \infty$  also called volume pairing. The general case is the density dependent  $\delta$ -interaction (DDDI). A typical value near matter equilibrium density  $\rho_{0,\text{pair}} = 0.16 \text{ fm}^{-3}$  concentrates pairing to the surface. This is often denoted as surface pairing. Allowing  $\rho_{0,\text{pair}}$  to be a free parameter of the model yields a value  $\rho_{0,\text{pair}} \approx 0.2 \text{ fm}^{-3}$  which puts the actual functional somewhere half way between volume and surface pairing [32]. A fully variational treatment of pairing yields the Hartree-Fock-Bogoliubov (HFB) equations. A widely used and robust simplification is the BCS approximation which suffices for all well bound nuclei [33]. All following calculations are done within the BCS scheme.

The space of pairing-active states has to be limited because the zero-range nature of the pairing functional (8) produces poor convergence with size of phase space. In numerical calculations only a moderately large set of states can be included. This is expressed by the phase-space weight  $w_\alpha$  in the definition (1) of the on-body density. Older recipes employ a sharp cutoff  $w_\alpha(\varepsilon_\alpha) = \theta(\varepsilon_{\text{cut}} - \varepsilon_\alpha)$ . This can be done in connection with large pairing spaces reaching up to 50 MeV above the Fermi surface [34]. Smaller spaces require a smooth cut off for which one often uses

$$w_\alpha = [1 + \exp((\varepsilon_\alpha - (\varepsilon_F + \varepsilon_{\text{cut}}))/\Delta\epsilon)]^{-1} \quad (9)$$

where typically  $\epsilon_{\text{cut}} = 5 \text{ MeV}$  and  $\Delta\epsilon = \epsilon_{\text{cut}}/10$  [35, 36]. The value  $\epsilon_\alpha$  is the single particle energy of the state  $\alpha$  and  $\epsilon_F$  is the chemical potential. This works very well for all stable and moderately exotic nuclei. For better extrapolation ability away from the valley of stability, the fixed margin  $\epsilon_{\text{cut}}$  is modified to use a band of fixed particle number  $\propto N^{2/3}$  instead of a fixed energy band [37].

#### 2.2.4. Correlation energy

Finally, we come to the correlation energy. It contains several contributions

$$E_{\text{corr}} = E_{\text{cm}} + E_{\text{rot}} + E_{\text{vib}} \quad , \quad (10)$$

a correction  $E_{\text{cm}}$  for the spurious center-of-mass energy, another term  $E_{\text{rot}}$  for rotational projection (non-zero only in deformed nuclei), and a term  $E_{\text{vib}}$  accounting for soft surface vibrations. The leading part which is used in practically all applications is  $E_{\text{cm}}$ . There exist several variants for it as summarized, e.g., in [13, 38, 39]. We use it here in the form

$$E_{\text{cm}} = \frac{\langle \hat{\mathbf{P}}_{\text{cm}}^2 \rangle}{2mA} \quad , \quad \hat{\mathbf{P}}_{\text{cm}} = \sum_{n=1}^A \hat{\mathbf{p}}_n \quad (11a)$$

which accounts for the effect of center-of-mass projection evaluated in second order Gaussian overlap approximation [40]. It employs, in fact, a two-body operator which makes its application in variational equations very cumbersome. It is thus only evaluated a posteriori, i.e. for the given solution of the SHF mean-field equations.

The rotational correction is, similar as  $E_{\text{cm}}$ , an approximation to rotational projection and looks

$$E_{\text{rot}} = \frac{\langle \hat{\mathbf{J}}^2 \rangle}{2\Theta} 2g\left(\left\langle \frac{\hat{\mathbf{J}}^2}{4} \right\rangle\right) \quad , \quad (12)$$

$$g(x) = x \partial_x \log \left( \int_0^1 dy e^{-x(1-y^2)} \right) \quad ,$$

where  $\hat{\mathbf{J}}$  is the operator of total angular momentum and  $\Theta$  the momentum of inertia as evaluated in the ATDHF approximation (also coined self-consistent Inglis inertia) [13, 41]. This rotational correction plays a crucial role for well deformed nuclei and should be included for them. The switch factor  $g$  serves to limit the correction to deformed nuclei and to leave (nearly) spherical nuclei untouched [41, 42, 43]. Similar as the c.m. correction  $E_{\text{cm}}^{(\text{full})}$ , it is a two-body operator and thus only evaluated a posteriori.

Finally,  $E_{\text{vib}}$  becomes noticeable in all nuclei with soft surface vibrations which are typically the transitional nuclei between spherical and well deformed ones. Its evaluation is very involved, for details see [41, 44, 45]. We will include the full correlation energies only once in the introductory overview in section 6.0.1. All further examples are confined to nuclei which are proven to have negligible vibrational-rotational corrections and need only  $E_{\text{cm}}$ .

#### 2.2.5. A comment on large amplitude motion

The correlation energies discussed in the previous section 2.2.4 are, in fact, covering effects beyond mean field. They are included for symmetry reasons (translation, rotation)

and because the (heavily fluctuating) correlations from low-energy vibrations cannot be embodied into a smooth energy functional. All three of these correlations are associated with low-energy, large-amplitude collective motion. There emerges now a subtle problem with extending the SHF functional to these cases. It is by definition a density functional, well defined only as expectation value over one mean-field state producing unambiguously one density matrix (1) and local densities therefrom. But the generator-coordinate method of large amplitude collective motion requires energy overlaps between different mean-field states [46]. These are a priori undefined for the SHF functional. One can motivate a unique extension to compute those overlaps which works well for center-of-mass projection [40]. But it was figured out later that one runs into subtle problems with the analytical structure of such an extended definition particularly in cases of particle-number projection [47], but also for rotational projection. Luckily enough, these problems are still absent when computing energy overlaps of mean-field states which stay still close to each other. And only these near overlaps are employed in modeling large-amplitude collective motion within the Gaussian overlap approximation to the generate-coordinate method [46]. All the correlations required here (see section 2.2.4) are evaluated in this limit and are thus at the safe side. The problem persists when full projection is necessary. One solution is to develop an effective energy functional which is developed consistently from an effective interaction. Work in this direction is in progress, see e.g. [48].

### 2.3. Motivation of the SHF functional

The standard pathway to derive an energy-density functional from ab-initio calculations is for electronic systems the much celebrated local-density approximation (LDA) [22] refined by non-local corrections through the generalized gradient approximation (GGA) [16]. This line of development is also a strong motivation for the nuclear case. But it cannot be simply copied for nuclear systems, first because nuclear ab-initio calculations are not yet as reliable as electronic ones are, and second, because nuclear energy functionals require more than mere density dependence as can be seen from the SHF functional (6). Although a quantitative derivation from ab-initio theories is still inhibited, at least the desirable formal structure of a Skyrme-like effective energy functional can be motivated by the technique of the density-matrix expansion [49, 50]. We sketch here the basic steps. For simplicity, we concentrate on the spatial part of the expansion and ignore spin-isospin structure. We also skip explicit vector notation.

Most ab-initio models deliver at the end an effective two-body interaction for an underlying mean-field calculation in terms of an involved integral operator, the  $T$ -matrix  $\hat{T}$ . An example is the Brueckner-Hartree-Fock method (BHF) whose  $T$ -matrix serves finally as effective force for the Hartree-Fock part, for reviews see e.g. [17]. An effective force as integral operator can also be extracted from other ab-initio models [31] as, e.g., the unitary correlator method. In any case, the most general total interaction

energy reads

$$E_{\text{pot}} = \int dx dx' dy dy' \varrho(x, x') T(x, x'; y, y') \varrho(y, y') \quad (13)$$

where  $\varrho(x, x')$  is the one-body density matrix (1). The key point is that  $\varrho(x, x')$  varies slowly with  $x, x'$  within a typical range of  $k_F^{-1}$  where  $k_F$  is the Fermi momentum. The  $T$ -matrix, on the other hand, is well concentrated in space, non-zero only for small differences in all pairs of coordinates with typical ranges mostly below  $k_F^{-1}$ . This suggests a Taylor expansion in all four coordinates  $x, x', y, y'$  about the common center  $R = (x + x' + y + y')/4$ . This reads up to second order

$$\begin{aligned} \varrho(x, x') \approx & \rho(R) + (\bar{x} - R) \nabla \rho|_R + \frac{1}{2} (\bar{x} - R)^2 \Delta \rho|_R \\ & + i(x - x') j|_R + \frac{1}{2} (x - x')^2 (\tau - \frac{1}{4} \Delta \rho)|_R \end{aligned} \quad (14)$$

where we abbreviate  $\bar{x} = (x + x')/2$ . A similar expansion holds for  $\varrho(y, y')$ . We insert this into the interaction energy (13) keep all terms up to second order in derivatives and recall that the  $T$ -matrix conserves parity as well as time-parity. This eliminates all terms of first order. What remains is just the SHF functional (6), of course, without the spin and spin-orbit terms which had been ignored in this quick “derivation”. The basic ingredient, the  $T$ -matrix, is assumed to stem from homogeneous matter and thus depends on the density for which it was evaluated. Thus all expansion coefficients  $C_T^{\text{type}}$  in the ansatz (6) carry, in principle, a density dependence. This is as far as we can get with formal reasoning. As argued above, we are still lacking sufficient information to fix all possible density dependencies and associate one only to the leading zeroth order terms  $\propto \rho_0^2$  and  $\propto \rho_1^2$ . This looks at first glance like a somewhat helpless escape. But it turns out to be a pragmatic and fruitful guess delivering a high-quality functional for many purposes, as we will see. The reason is that the density of nuclei gathers predominantly around the equilibrium density  $\rho_0 \approx \rho_{\text{eq}}$  due to strong nuclear saturation.

Altogether, the density-matrix expansion demonstrates how a zero-range effective interaction emerges naturally from the initially given involved operator structure. We are dealing with a typical low-energy or low- $q$  expansion [51]. It requires that the spatial structure should be sufficiently smooth which means in the present case that the essential physics of the  $T$ -matrix is concentrated at length scales smaller than the typical wavelength  $k_F^{-1}$ . This is fine at normal nuclear density. But one should warned with extensions to high densities. Sooner or later, effective functionals of zero range will become inappropriate although the validity of effective functionals exceeds often the range of such safe estimates.

### 3. Observables

#### 3.1. Homogeneous nuclear matter

Although not experimentally accessible, homogeneous nuclear matter is an extremely useful system to characterize basic nuclear properties. Nuclear matter properties (NMP) have been used over decades as key parameters in macroscopic models [5, 52, 53]. Extensive studies in

this domain have developed reliable, although model dependent, values for them. It is technically simple for every mean-field model to compute NMP for homogeneous matter. Moreover, NMP can be given a physical interpretation. Thus NMP are helpful quantities to characterize a model and to compare different models. We introduce here those NMP which will be used in the following.

Homogeneous nuclear matter is to be taken without Coulomb force (it can be assumed to be neutralized by a homogeneous electron background), pairing, and c.m. correction. It remains the energy per particle as

$$\frac{E}{A}(\rho_0, \rho_1, \tau_0, \tau_1) = \frac{\mathcal{E}_{\text{kin}} + \mathcal{E}_{\text{Sk}}}{\rho_0} \quad (15)$$

where we consider for a while  $\rho$  and  $\tau$  as independent variables. We keep the independence just to allow a simple computation of effective masses. Of course, a given system is characterized just by the densities  $\rho_T$  and the kinetic density depends on these given densities as  $\tau_T = \tau_T(\rho_0, \rho_1)$ . Thus we have to distinguish between partial derivatives  $\partial/\partial\tau$  which take  $\tau_T$  as independent and total derivatives  $d/d\rho$  which know only the  $\rho_T$  dependence. The relation is

$$\frac{d}{d\rho_T} = \frac{\partial}{\partial\rho_T} + \sum_{T'} \frac{\partial\tau_{T'}}{\partial\rho_T} \frac{\partial}{\partial\tau_{T'}} \quad (16)$$

The standard NMP are defined at the equilibrium point ( $\rho_0 = \rho_{\text{eq}}, \rho_1 = 0$ ) of symmetric nuclear matter. They are summarized in table 1. Most of the NMP are obvious.

A few remarks on two more subtle features: The slope of symmetry energy  $L$  characterizes the density dependence of the symmetry energy which allows to estimate the symmetry energy at half density, i.e. at surface of finite nuclei. The enhancement factor for the Thomas-Reiche-Kuhn (TRK) sum rule [33] is a widely used way to characterize the isovector effective mass which is obvious from the given expression involving derivative with respect to  $\tau_1$ .

The NMP in table 1 can be grouped into four classes: first, the (isoscalar) ground state properties  $\rho_{\text{eq}}$  and  $E/A|_{\text{eq}}$ , second, isoscalar response properties  $K$  and  $m/m_*$ , and third, isovector response properties  $J, L, \kappa_{\text{TRK}}$ . The response properties determine zero sound in matter [55] and subsequently they are closely related to giant resonance modes in finite nuclei as we will see later. There is a fourth category, the surface energies which go already beyond homogeneous matter and are explored in the surface of semi-infinite matter. Their computation in the context of quantum mechanical mean-field theories is involved [54]. But they are an important ingredient in macroscopic models and thus should also be checked in mean-field theories.

It is to be noted that the nine NMP in table 1 taken together are fully equivalent to the nine model parameters in the SHF functional (6), namely  $C_T^\rho, C_T^{\rho,\alpha}, \alpha, C_T^\tau$ , and  $C_T^{\Delta\rho}$ . There is a one-to-one correspondence between the both sets. This allows to consider the NMP also as model parameters. This is a more intuitive way to communicate the model parameters and it allow direct comparison with other mean-field models which are often also fully mappable to NMP, see for example the comparison of symmetry energies in [56].

isoscalar ground state properties		
equilibrium density:	$\rho_{\text{eq}} \leftrightarrow$	$\frac{d}{d\rho_0} \frac{E}{A} \Big _{\text{eq}} = 0$
equilibrium energy:	$\frac{E}{A} \Big _{\text{eq}}$	
isoscalar response properties		
incompressibility:	$K_\infty =$	$9\rho_0^2 \frac{d^2}{d\rho_0^2} \frac{E}{A} \Big _{\text{eq}}$
effective mass:	$\frac{\hbar^2}{2m^*} =$	$\frac{\hbar^2}{2m} + \frac{\partial}{\partial \tau_0} \frac{E}{A} \Big _{\text{eq}}$
isovector response properties		
symmetry energy:	$J =$	$\frac{1}{2} \frac{d^2}{d\rho_1^2} \frac{E}{A} \Big _{\text{eq}}$
slope of $J$ :	$L =$	$\frac{3}{2} \rho_0 \frac{d}{d\rho_0} \frac{d^2}{d\rho_1^2} \frac{E}{A} \Big _{\text{eq}}$
TRK sum-rule enh.:	$\kappa_{\text{TRK}} =$	$\frac{2m}{\hbar^2} \frac{\partial}{\partial \tau_1} \frac{E}{A} \Big _{\text{eq}}$
surface properties (semi-infinite matter)		
surface energy:	$a_{\text{surf}}$	see [54]
surface symm. en.:	$a_{\text{surf,sym}}$	see [54]

Table 1: Definition of the nuclear matter properties (NMP). All derivatives are to be taken at the equilibrium point of symmetric nuclear matter.

Pure neutron matter is also an important system as there exists an actual realization in neutron stars. Thus we will look occasionally at the neutron equation-of-state (EoS)  $E/A|_{\text{neut}}(\rho)$  which is key input to the computation of neutron star properties, see figure 3. A way to characterize the EoS by one relevant number is to look at the slope of the EoS at a typical density. This is  $d/d\rho E/A|_{\text{neut}}$  taken at  $\rho = 0.1 \text{ fm}^{-3}$ . This observable shows up amongst others in figure 14 which shows that this observable (as most of the neutron EoS) is strongly related to static isovector response.

### 3.2. Finite nuclei

The most prominent observables described by an energy-density functional are, of course, energy and density. Total binding energy  $E_B$  is computed in straightforward manner with eq. (6). Although the local densities (2) are immediately available as ingredients of the mean-field calculations, its relation to measurement is more involved and deserves some explanation.

From the experimental side, only the charge density is easily accessible through elastic electron scattering which allows a more or less model free determination of the nuclear charge formfactor  $F_C(\mathbf{k})$  [57]. From the theoretical

side, the charge formfactor is computed as [58]

$$F_C(k) = \sum_{q \in \{p,n\}} [F_q G_{E,q} + F_{ls,q} G_M] \exp\left(\frac{\hbar^2 k^2}{8 \langle \hat{\mathbf{P}}_{\text{cm}}^2 \rangle}\right), \quad (17)$$

$$F_q(\mathbf{k}) = \int d^3r \exp i\mathbf{k} \cdot \mathbf{r} \rho_q(\mathbf{r}),$$

where  $F_{ls,q}$  is the form factor of  $\nabla \cdot \mathbf{J}_q$  augmented by a factor  $\mu_q/4m^2$  with  $\mu_q$  being the magnetic moment of the nucleon,  $G_{E,q}$  is the electric form factor and  $G_M$  the magnetic form factor of the nucleons (assumed to be equal for both species). The overall exponential factor takes into account the center-of-mass correction for the formfactor complementing the corresponding energy correction (11). It employs the same variance of the total momentum  $\langle \hat{\mathbf{P}}_{\text{cm}}^2 \rangle$  and its physical interpretation is an unfolding of the spurious vibrations of the nuclear center-of-mass in harmonic approximation [40]. The nucleon form factors  $G_{E,q}$  and  $G_M$  are taken from nucleon scattering data [59, 60], for details see [13].

Exact DFT should, in principle, provide a reliable description of density distributions, or formfactors respectively, in all details [22]. However, actual functionals employ analytically simple forms which are smooth functions of the densities as motivated by a local-density approximation. It has been shown that this limits the predictive value to the regime  $k < 2k_F$  in the formfactor where  $k_F$  is the Fermi momentum [61]. Fortunately, the most crucial bulk properties of the nuclear density profile are determined at low  $k$ . These are [57]

charge r.m.s. radius:

$$r_C = \frac{3}{F_C(0)} \frac{d^2}{dk^2} F_C(k) \Big|_{k=0}$$

charge diffraction radius:

$$R_C = \frac{4.493}{k_0^{(1)}} \quad , \quad F_C(k_0^{(1)}) = 0 \quad (18)$$

charge surface thickness:

$$\sigma_C = \frac{2}{k_m} \log \left( \frac{F_{\text{box}}(k_m)}{F_C(k_m)} \right)$$

$$F_{\text{box}}(k) = 3 \frac{j_1(kR_C)}{kR_C} \quad , \quad k_m = \frac{5.6}{R_C} \quad ,$$

where  $k_0^{(1)}$  is the first zero of the formfactor  $F_C$ . The diffraction radius  $R_C$  parametrizes the overall diffraction pattern which resembles those of a filled sphere of radius  $R_C$  [57]. The actual nuclear formfactor decreases faster than the box formfactor  $F_{\text{box}}$  due to the finite surface thickness  $\sigma_C$  of nuclei which is thus determined by comparing the height of the first maximum of the box equivalent formfactor and of the mean-field result  $F_C$ .

Binding energy  $E_B$  and the three bulk parameters (18) of the charge formfactor are the key observables in the pool of fit data, see section 4.1. Besides these bulk properties, we also include in the fit pool odd-even staggering of binding energies to fix the pairing strength. It reads for neutrons

$$\Delta_n^{(3)}(Z, N) = \frac{1}{2} (E_B(Z, N+1) - 2E_B(Z, N) + E_B(Z, N-1)) \quad (19)$$

and similarly for protons. It is interesting to note that the odd-even staggering also refers to binding energies. But taking the difference of them filters a much different information than the one seen in binding energies as such. Moreover we consider for the fits a few selected spin-orbit splittings in the spectrum of s.p. energies  $\Delta\epsilon_{nl} = \epsilon_{nlj-\frac{1}{2}} - \epsilon_{nlj+\frac{1}{2}}$  to fix the strength of the spin-orbit term.

Binding energy  $E_B$  is also considered for nuclei outside the fit pool as predicted (or extrapolated) observables, e.g., when estimating the properties of exotic nuclei and super-heavy elements. Very useful are also differences of binding energies as two-nucleon separation energies or the energy expense for  $\alpha$ -decay

$$Q_\alpha = E_B(Z, N) - E_B(N-2, Z-2) - E_B(2, 2) \quad . \quad (20)$$

Differences act as amplifying glass. They subtract smooth bulk properties and can reveal other aspects of a model as mentioned already in connection with the  $\Delta_{p/n}^{(3)}(Z, N)$ . We will see that also when discussing statistical correlations between observables in section 6.5.

The charge distribution is mostly sensitive to the proton distribution. Unfortunately, experimental information on neutron or mass density is plagued with model dependence [62]. Promising measurements of neutron radii with high-energy particle scattering are coming up [63, 64], but have yet to become more precise. It is worth the effort because reliable information on neutron radii will be of invaluable help to assess isovector properties of the nuclear functional [65]. Thus we will have a look also at the neutron radius  $r_n$  in the following. We do this in terms of the neutron skin from r.m.s. radii

$$r_{\text{skin}} = r_n - r_p \quad . \quad (21)$$

Taking the difference of two similar bulk properties acts, again, as an amplifying glass which filters particularly the isovector properties.

SHF is also adapted to deal with nuclear excitations. The most prominent ones are the much celebrated giant resonances. They are usually described by the random-phase approximation (RPA), a dynamical self-consistent mean-field theory of small-amplitude oscillations see, e.g., [33]. We treat it here with the efficient operator techniques of [66, 67]. RPA delivers the full spectral strength distribution. For the analysis in this paper, it is preferable to have one number to characterize an excitation. Giant resonances in heavy nuclei are the perfect candidates for that because their spectrum is well concentrated in one resonance. Thus we will consider in the following as a measure for typical resonance excitation properties the peak energies of the isoscalar giant monopole resonance (GMR), the isovector giant dipole resonance (GDR), and the isoscalar giant quadrupole resonance (GQR), all in  $^{208}\text{Pb}$ . The GMR and GQR are very well concentrated and thus can be safely computed by the inexpensive fluid-dynamical approximation [67]. The GDR has a somewhat broader, though still peaked, distribution and requires full RPA for correctly placing the resonance peak. We take here the point of view that the giant resonances are well described by time-dependent mean-field theory at the level of RPA. We have to mention, however, that it is still a matter of debate whether this description suffices. There are

calculations including complex configurations (coupling to phonons) which indicate that such many-body correlations modify the giant resonances [68]. Fortunately, they do that mainly for the width of the resonance. But some effects on the peak position cannot be excluded. Another problem is that the trend of peak positions towards lighter nuclei is not correctly reproduced by SHF-RPA [69]. It is not yet clear whether this points to a weakness of modeling isovector density dependence or whether it becomes another argument in favour of many-body correlations in the giant resonances [70]. Thus there are still open question in the theoretical description of giant resonances. At present, we adopt the view that RPA provides relevant peak positions, at least for heavy nuclei. We will thus consider the resonances in  $^{208}\text{Pb}$ .

There is another crucial number which can be extracted from the dipole strength distribution, the isovector dipole polarizability  $\alpha_D$ . Just recently, there came up very careful experimental evaluations which deliver  $\alpha_D$  with high precision [71, 72]. This is thus a welcome data point to assess static isovector response in mean-field models. The polarizability can be evaluated as integral over the dipole strength with inverse energy weight. This is the standard way in experimental evaluation and an option in theoretical calculation. Mean-field theory allows an even more robust access as the static response to an external dipole field. To that end, one computes the nuclear ground state with a small additional dipole field  $V_{\text{ext}} = \lambda \hat{d}$  where  $\hat{d}$  is the isovector dipole operator. The polarizability is then deduced from the dipole response of the system  $\alpha_D = \partial/\partial\lambda \langle \hat{d} \rangle$ . In our calculation, we use this robust and inexpensive option.

We will also consider fission barriers in super-heavy elements. The fission path is computed by quadrupole constrained SHF as a series of mean-field states  $\Phi_{\alpha_{20}}$  with systematically increasing quadrupole momentum  $\alpha_{20}$ . This yields the collective potential for fission as  $\mathcal{V}(\alpha_{20}) = E_{\text{SHF}}(\Phi_{\alpha_{20}})$ . It has to include the full correlation energy (10). The fission barrier is then

$$B_f = \mathcal{V}_{\text{max}} - \mathcal{V}_{\text{min}} + E_{\text{coll},0} \quad (22)$$

where  $\mathcal{V}_{\text{max}}$  is the potential at the peak of the barrier,  $\mathcal{V}_{\text{min}}$  at the minimum, and  $E_{\text{coll},0}$  is the energy of the collective ground state above  $\mathcal{V}_{\text{min}}$ . The  $E_{\text{coll},0}$  defines the entry point for fission as it is explored in experiment. Note that we thus include for this observable some correlation effects beyond SHF which means that  $B_f$  is not a pure mean-field observable. For details of this rather involved definition and calculations see [73, 74]. An extensive discussion of fission properties in connection with statistical analysis is found in [75]. Here we spot only one example.

We will also have a look at low-lying quadrupole vibrations (lowest  $2^+$  states). These are related to large amplitude motion in mid-shell nuclei and thus treated very similar to fission. One generates a collective path with systematically changed quadrupole deformation thus mapping the collective potential  $\mathcal{V}(\alpha_{20})$  for quadrupole motion. The potential is augmented by a collective mass to be computed by self-consistent cranking mass (often called AT-DHF mass) and correction for the spurious zero-point energy. This together defines a collective Schrödinger equation whose solution then yields the collective excitation

energies and associated B(E2) values. For details of this rather involved formal framework see, e.g., [41, 46].

## 4. Calibration of the model and analysis of predictive power

### 4.1. Least-squares fit

We have used in section 2.3 some formal reasoning to motivate the form of the SHF functional (6). The actual values of the parameters  $C_T^{(\text{type})}$  remain open. Up to now, there exists no quantitatively successful derivation of the parameters from ab-initio calculations and this will remain so for a while because the case of nuclear many-body theory is not yet unambiguously settled. It is standard practice since decades to calibrate the SHF functional (and competing mean-field models) to empirical data. Various strategies have been used for that in the past. The most systematic approach is probably a least-squares ( $\chi^2$ ) fit [76] which was used in an SHF context first in [77] and has meanwhile become the standard method for calibration of self-consistent mean-field models. There remains a great variety in the bias set by the choice of empirical data for a fit. To name a few examples out of many: some concentrate on spherical nuclei with negligible correlation effects [32], others are particularly concerned with deformed nuclei [78, 79, 80], still others try to adjust also spectra of s.p. energies [81, 82]. The properties of the resulting functionals have much in common, although some differences may be found in details. This indicates some robustness of the modeling. We will discuss in section 6.2 the impact of variations of fit data. The standard pool of fit data for this publication will be explained at the end of this section. Before that, we briefly summarize the  $\chi^2$  technique.

Center piece of  $\chi^2$  fits is a global quality measure by summing the squared deviations from the data as

$$\begin{aligned}\chi^2 &= \sum_{\text{obs}} \chi_{\text{obs}}^2, \\ \chi_{\text{obs}}^2 &= \sum_{\text{nucl}} \frac{\mathcal{O}_{\text{obs,nucl}}^{(\text{th})} - \mathcal{O}_{\text{obs,nucl}}^{(\text{exp})}}{\Delta \mathcal{O}_{\text{obs,nucl}}},\end{aligned}\quad (23)$$

where  $\mathcal{O}$  stands for an observable, “obs” for a type of observables ( $E$ ,  $r_{\text{rms}}$ , ...), “nucl” for a nucleus (defined by  $Z, N$ ), the upper index “th” for a calculated value, and “exp” for the experimental value. The denominator  $\Delta \mathcal{O}_{\text{obs,nucl}}$  quantifies the adopted error of that observable. It renders each contribution dimensionless and regulates the relative weights of the various terms. It is to be noted that  $\Delta \mathcal{O}_{\text{obs,nucl}}$  cannot be identified with the experimental error on the given observable which is usually much smaller. The limiting factor are limitations at the side of the model, i.e., the quality we can expect from a mean-field description. A self-regulating choice is to tune all  $\Delta \mathcal{O}_{\text{obs,nucl}}$  in one group “obs” the same way such that  $\chi_{\text{obs}}^2$  yields in the average a contribution of about one for each nucleus [76, 83], for details in the nuclear context see [84].

The total quality measure is a function of all model parameters, i.e.  $\chi^2 = \chi^2(\mathbf{p})$  where  $\mathbf{p} = (p_1, \dots, p_F)$ . The

optimal parameters  $\mathbf{p}_0$  are those which minimize  $\chi^2$ , i.e.

$$\mathbf{p}_0 : \quad \chi^2(\mathbf{p}_0) = \chi_0^2 = \min. \quad (24)$$

The minimum condition looks straightforward. But finding the absolute minimum is a non-trivial task because the  $\chi^2$  landscape has several minima and often discontinuities in between [26]. We employ the minimization technique from Bevington [76] which works well in the vicinity of minima and combine that with Monte-Carlo steps to explore the rough  $\chi^2$  landscape in a broader range. For large scale searches, there are more elaborate methods around, e.g. more robust iteration to a minimum [85] or genetic algorithms for particularly obstinate cases [86].

Finally, we comment briefly on the choice for the pool of fit data used later on. Some more details are provided in appendix B. We are using exactly the same data as in the survey of [32]. In that paper, the experimental values and the adopted errors are explained in great detail. Thus we need not to repeat it here. The set of fit data includes the bulk properties  $E_B$ ,  $r_{\text{rms}}$ ,  $R_{\text{diff}}$ , and  $\sigma$  plus pairing gaps and some spin-orbit splittings (see section 3.2). The nuclei are restricted to be spherical and carefully selected to have small ground-state correlations [41]. This guarantees that we deal with nuclei which can reliably well be described by a mean-field model. Another group which has small correlation effects would be strongly deformed nuclei. We omit them for practical reasons because they are costly to compute. All transitional nuclei require corrections from vibrational correlations and must be discarded from any fit pool.

### 4.2. Statistical error analysis

Not only the optimal parametrization  $\mathbf{p}_0$ , but also the parameters in the vicinity of  $\mathbf{p}_0$  deliver a reasonable reproduction of data. This is systematically quantified in statistical analysis [76, 83]. Although we will see later that the residual errors  $\mathcal{O}_{\text{obs,nucl}}^{(\text{th})} - \mathcal{O}_{\text{obs,nucl}}^{(\text{exp})}$  (also called simply “residuals”) in  $\chi^2$  fits of nuclear mean-field models are not really statistically distributed, we will employ the well developed schemes of statistical analysis for estimating extrapolation errors and correlations between observables. It remains in any case a powerful tool to explore the  $\chi^2$  landscape and the information it contains about the interplay of model and fit data.

Assuming a statistical distribution of residuals, one postulates a probability distribution of reasonable model parameters as [83, 87]

$$W(\mathbf{p}) \propto \exp(-\chi^2(\mathbf{p})) \quad (25)$$

Their domain is characterized by  $\chi^2(\mathbf{p}) \leq \chi_0^2 + 1$  (see Sec. 9.8 of Ref. [83]). The range of  $\mathbf{p}$  fulfilling this condition is usually small and we can perform a Taylor expansion

$$\chi^2(\mathbf{p}) \approx \chi_0^2 + \sum_{\alpha, \beta=1}^{N_p} (p_\alpha - p_{0,\alpha})(\mathcal{C}^{-1})_{\alpha\beta}(p_\beta - p_{0,\beta}), \quad (26)$$

$$(\mathcal{C}^{-1})_{\alpha\beta} = \left. \frac{1}{2} \partial_{p_\alpha} \partial_{p_\beta} \chi^2 \right|_{\mathbf{p}_0} \simeq \sum_i J_{i\alpha} J_{i\beta}, \quad (27)$$

$$J_{i\alpha} = \left. \frac{\partial_{p_\alpha} \mathcal{O}_i}{\Delta \mathcal{O}_i} \right|_{\mathbf{p}_0}, \quad (28)$$



where  $\hat{J}$  is the rescaled Jacobian matrix and  $\mathcal{C}$  the covariance matrix. The latter plays the key role in covariance analysis. The domain of reasonable parameters is thus given by

$$\chi^2(\mathbf{p}) - \chi_0^2 \approx \mathbf{p} \cdot \hat{\mathcal{C}}^{-1} \cdot \mathbf{p} \leq 1 \quad (29)$$

which defines a confidence ellipsoid in the space of model parameters. It is related to the Taylor expanded probability distribution (25) which becomes

$$W(\mathbf{p}) = \left[ (2\pi)^F \det\{\hat{\mathcal{C}}\} \right]^{-1/2} \exp\left(-\frac{1}{2} \mathbf{p} \cdot \hat{\mathcal{C}}^{-1} \cdot \mathbf{p}\right) \quad (30)$$

where the fore-factor guarantees proper normalization  $\int d^F p W = 1$ .

Any observable  $A$  is a function of model parameters  $A = A(\mathbf{p})$ . The value of  $A$  thus varies within the confidence ellipsoid, and this results in some uncertainty  $\Delta A$ . Usually, one can assume that  $A$  varies weakly such that one can linearize it

$$A(\mathbf{p}) \simeq A(\mathbf{p}_0) + \mathbf{G}^A \cdot (\mathbf{p} - \mathbf{p}_0) \quad , \quad (31a)$$

$$\mathbf{G}^A = \left. \partial_{\mathbf{p}} A \right|_{\mathbf{p}_0} . \quad (31b)$$

This together with the Gaussian probability distribution (30) allows to compute analytically averages and variances. The average becomes

$$\bar{A} = \int d^F p W(\mathbf{p}) A(\mathbf{p}) = A(\mathbf{p}_0) \quad (32a)$$

as one would have expected. The variance quantifies the fluctuation of  $A$  around  $A(\mathbf{p}_0)$  and is

$$\begin{aligned} \overline{\Delta A} &= \sqrt{\overline{\Delta^2 A}} , \\ \overline{\Delta^2 A} &= \int d^F p W(\mathbf{p}) (A(\mathbf{p}) - \bar{A})^2 \\ &= \sum_{\alpha\beta} G_{\alpha}^A \mathcal{C}_{\alpha\beta} G_{\beta}^A , \end{aligned} \quad (32b)$$

with  $G_{\alpha}^A$  as given in eq. (31b). As it is derived from a statistical interpretation of the  $\chi^2$  landscape, it is also coined statistical error. Along the same lines, one can also define a cross-variance between two different observables. It reads

$$\begin{aligned} \overline{\Delta A \Delta B} &= \int d^F p W(\mathbf{p}) (A(\mathbf{p}) - \bar{A})(B(\mathbf{p}) - \bar{B}) \\ &= \sum_{\alpha\beta} G_{\alpha}^A \mathcal{C}_{\alpha\beta} G_{\beta}^B \end{aligned} \quad (32c)$$

This then allows to define the covariance, or correlation coefficient,

$$c_{AB} = \frac{|\overline{\Delta A \Delta B}|}{\overline{\Delta A \Delta A} \overline{\Delta B \Delta B}} . \quad (32d)$$

It quantifies the statistical correlations between two observables  $A$  and  $B$ . A value  $c_{AB} = 1$  means fully correlated where knowledge of  $A(\mathbf{p})$  fully determines  $B(\mathbf{p})$ . A value  $c_{AB} = 0$  means uncorrelated, i.e.  $A(\mathbf{p})$  and  $B(\mathbf{p})$  are statistically independent where knowledge of  $A(\mathbf{p})$  carries no information whatsoever on  $B(\mathbf{p})$ , for examples see [88, 89].

## 5. Strategies for estimating errors

Although very powerful, a  $\chi^2$  fit is a black box and seduces the user to use it without much understanding of the physics beyond. One plugs in a model, chooses a couple of relevant fit data, and grinds the mill until one is convinced to have found the absolute minimum  $\chi_0^2$  together with the optimal parameters  $\mathbf{p}_0$ . Thus far one may find a satisfying description of the fit data but may live with little understanding of the relevance and reliability of the model. The challenging task remains to understand the model thus achieved, in particular its reliability in extrapolations to other observables. This is the quest for error estimates, see [84] for a basic discussion of error estimates in the context of nuclear models. The problem does not have a simple and unique answer. Statistical errors as explained in section 4.2 are well under control. The hard part is to estimate the systematic errors coming from prejudices in the modeling or choice of data. The bad news is that there is no systematic way to assess systematic errors. From a critical point of view, every physical theory holds only preliminarily and is always threatened by hidden insufficiencies which may be revealed some days by new observations. As a consequence, we need to handle our theories with a great deal of restless error awareness. The best way to enhance confidence in a model is to scrutinize it employing a great variety of different checks and so piece-wise put together a view of the sources of uncertainty. In the following, we summarize a couple of possible checks:

### 1. Exploring a model from the theoretical side

#### 1. Estimates of beyond mean-field effects:

The first step at all is to check whether the model under consideration is appropriate to describe the wanted data. This means for SHF to check many-body correlations beyond mean field. Density matrix expansion (see [49, 50] and section 2.3) indicates that short-range correlations can be mapped into an energy functional. However, correlations from low lying  $2^+$  states fluctuate strongly and cannot be mapped into a smooth functional. Nuclei which acquire large correlation corrections should be excluded from the pool of fit data [32, 41]. The search for possible correlation effects has not yet come to an end, for an example see section 6.4.

#### 2. Exploring the stability of the model:

Models which rely on expansions are likely to have regions of instability. There is also the problem that  $\chi^2(\mathbf{p})$  can have non-analytical points. It is crucial to explore those dangerous regimes and set rules to avoid them, or to cure the problem. These considerations have accompanied the development of SHF all along, for recent critical studies, particularly of the tensor term, see [26, 27, 28, 29].

#### 3. Formal analysis of inter-dependencies:

Correlation analysis (see point 2.2) can reveal dependencies between observables. To make sure that these are more than statistical correlations, one ideally establishes the connection at

a purely formal level. Literature on such studies is unoverseeable. We mention here only two examples, one for the relation between effective mass  $m^*/m$  and level density [90] and another one for the mapping of SHF parameters to NMP via the LDM [91].

#### 4. Variations of the functional:

A test for a model from within is to vary the basic ansatz. This means, e.g., for the SHF model to omit or to add terms or to vary the density dependence [92]. Another way is to compare and/or accumulate the results from different models as done by combination with RMF in [89, 93]. We will exemplify in section 6.1 adding and omitting terms.

## 2. Straightforward statistical analysis

#### 1. Extrapolation uncertainties:

This employs eq. (32b) to estimate the statistical error on extrapolations. It serves as useful indicator for safe and unsafe regions of the model see, e.g., section 6.0.2.

#### 2. Correlations between observables:

The covariances (32d) reveal dependencies between observables. This helps to estimate the information content of a new measurement, for examples see [88] and section 6.5. It may be combined with a variation of fit data (see point 3.3) to distinguish between model properties and data dependence. It can also serve to motivate searches for formal connections (see point 1.3).

#### 3. Sensitivity of model parameters $\mathbf{p}$ :

The Jacobian matrix  $\hat{J}$  together with the covariance matrix  $\hat{C}$  allows to explore the impact of each single model parameter  $p_\alpha$  on a given fit observable  $\hat{O}_i$ . Examples are found in [80, 84, 85].

## 3. Exploring the model by dedicated variations

#### 1. Unresolved trends of residual errors:

A perfect model should produce a purely statistical (Gaussian) distribution of residuals  $\mathcal{O}_{\text{obs,nucl}}^{(\text{th})} - \mathcal{O}_{\text{obs,nucl}}^{(\text{exp})}$ . Well visible trends of residuals of one sort of observable over the series of nuclei indicate deficiencies of the model. All nuclear mean-field models produce still strong unresolved trends see, e.g., [32, 69, 85] and section 6.0.1.

#### 2. Dedicated variations of parameter or observable:

As a complement to correlation analysis (see point 2.2), one obtains a direct view of dependencies by dedicated variation of a parameter  $p_\alpha$  or observable  $A(\mathbf{p})$ . To that end, one fits a parametrization with constraint on a fixed value of  $p_\alpha$  or  $A$  and systematically varies the constrained value [32]. Then one looks at the trend of other observables  $B(p_\alpha)$ , or  $B(A)$  respectively. This test is particularly instructive when using variations of NMP, see [32] and section 6.3.

#### 3. Variations of fit data:

The fit observables  $\hat{O}_{\text{obs,nucl}}$  stem from different

groups of observables “obs” as, e.g., energy or radius. One can omit a group from the pool of fit data. Comparison with the full fit allows to explore the impact of the omitted group, see [94] and section 6.2.

#### 4. Test of predicted observables:

A natural test is to compare a prediction (extrapolation) with experimental data wherever available. It is a strong indicator for a systematic error if the deviation exceeds significantly the extrapolation error (32b). An example for such a critical case is the energy of super-heavy nuclei where systematic deviations point to a problem of SHF, see [69] and section 6.0.1.

The above list of testing strategies shows that establishing a model requires a broad palette of tools and counterchecks. The present paper can not exemplify all of them. We will address the groups 2 and 3 as well as point 1.4 from group 1.

## 6. Results

### 6.0.1. Bulk properties

Modern SHF parametrization have reached a high quality of reproduction of nuclear ground state properties. As example, we quote here the r.m.s. errors for SV-min which was fitted to ground state properties of semi-magic spherical nuclei [32]. They are 0.6 MeV for binding energies  $E_B$ , 0.029 fm for charge diffraction radii  $R_{\text{diff}}$ , 0.022 fm for charge surface thicknesses, and 0.017 fm for charge r.m.s. radii. Similar quality is found for all modern parametrizations which appeared in the last decade.

Although small, the question is how the errors are distributed over the nuclei. We do that here for SV-min [32]. Figure 1 shows the residuals  $\mathcal{O}_{\text{obs,nucl}}^{(\text{th})} - \mathcal{O}_{\text{obs,nucl}}^{(\text{exp})}$  of r.m.s. radii (upper panel) and of binding energies (middle and lower panel) for all nuclei for which data were available. Different symbols (and colors) distinguish nuclei from the fit pool, well deformed nuclei, and everything else. The lower panel shows binding energies  $E_B$  from SHF calculations with c.m. correction, but without any other correlation correction (10). The fit nuclei gather nicely within a small error band as given by the above mentioned r.m.s. errors. That is no surprise because they were selected to have negligible correlations [32, 41]. The other nuclei deviate significantly. The middle panel shows the results with all corrections from collective correlations, see eq. (10). This brings all results closer to a narrow error band. The deformed nuclei in the medium heavy region ( $A < 200$ ) perform already very well while transitional nuclei still overshoot.

The errors are obviously not statistically distributed but show strong trends which are not resolved by the given SHF model. Even with correlation corrections (middle panel) errors are smallest towards shell closures and largest in between, particularly for the transitional nuclei (red triangles). This is clearly a shell fluctuation not fully accounted for by the present estimate of correlations (only from the lowest  $2^+$  state). More than that, there is a strong trend to underbinding with increasing system

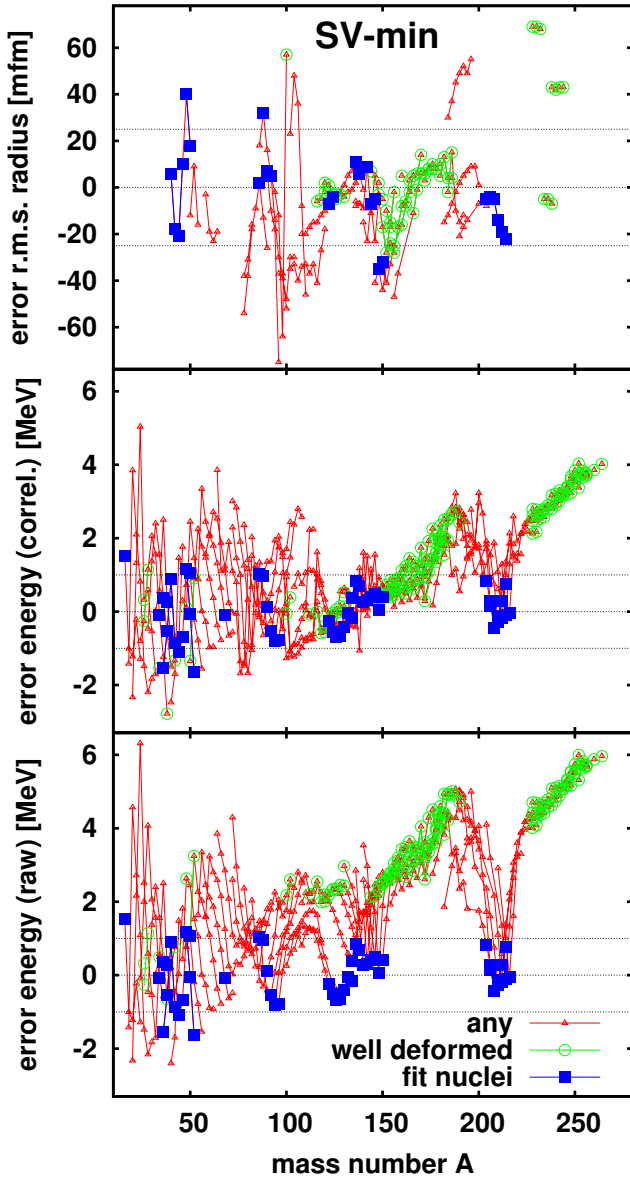


Fig. 1: Deviations of SHF calculations from experimental data for all nuclei for which data were available. Fit nuclei are shown with filled blue squares, well deformed nuclei with green circles, and all other with red triangles. Isotopic chains are connected by a line. Lower panel: for binding energies computed with (deformed) SHF including only the c.m. correction. Middle panel: for binding energies with SHF plus corrections from collective correlations (vibration and rotation). Upper panel: For charge r.m.s. radius computed with (deformed) SHF.

size  $A$  for deformed nuclei (green circles). This becomes obvious in the regime of actinides and super-heavy elements ( $A > 220$ ). Even attempts with variations of density dependence [92] and including deformed nuclei in the fit [69] could not resolve the problem. It seems to be inherent in the way the present SHF functional (6) models density dependence. For example, traditional RMF functionals which model density dependence quite differently by non-linear self-coupling of the  $\sigma$  meson have the opposite problem: they tend to overbind super-heavy nuclei [95]. The unwanted trends in figure 1 suggest that there is still a need for improvement in nuclear self-consistent mean-field models.

The upper panel shows deviations for charge r.m.s.

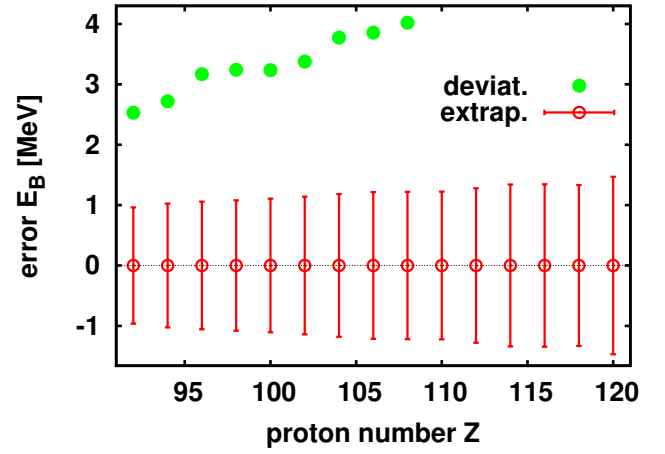


Fig. 2: Evolution of errors for a chain of super-heavy elements with increasing proton number  $Z$  in steps of 2. The neutron number has been increased accordingly in steps of 4, occasionally steps of 2, to cover the landscape of super-heavy elements ending up near the magic neutron number  $N = 184$ . Shown are extrapolations errors (denoted “extrap.”) and deviations from data  $E_{\text{SHF}} - E_{\text{exp}}$  (denoted “deviat.”) where  $E_{\text{SHF}}$  includes correlation corrections as explained in connection with figure 1. The parametrization SV-min was used.

radii. Correlation effects are smaller for this observable and not shown. There are also less data which leads to less points on the plot. The deviations gather better within the error band from the fit nuclei. Nonetheless, they are also not statistically distributed. We observe again the shell fluctuations between shell closure and mid-shell nuclei. The pronounced trend for deformed, super-heavy nuclei which was seen for binding energies is absent for r.m.s. radii.

### 6.0.2. Far extrapolations

An important quantity delivered by the  $\chi^2$  technique is the variance (32b) of an observable. It provides an estimate for the extrapolation uncertainty which is extremely useful to get an impression how reliable an extrapolation may be. We exemplify that here for an extrapolation to super-heavy nuclei and an extremely far extrapolation to neutron star properties. The case of super-heavy nuclei continues the discussion from the previous section 6.0.1 of an unresolved trend for heavy nuclei.

Figure 2 shows extrapolation uncertainties computed with eq. (32b) and actual deviations from data (where available) computed with SV-min for a chain of super-heavy nuclei from  $Z = 90$  to  $Z = 120$ . The sequence of neutron numbers has been chosen to cut a path through the landscape spanning from  $Z/N=90/126$  to  $120/182$ . It was:  $N = 126, 130, 134, 138, 142, 146, 148, 150, 152, 154, 158, 162, 166, 170, 174, 178$ , and  $182$ . The extrapolation uncertainties (shown as error bars) grow steadily when moving away from the region of fit nuclei. This is an expected behavior: the farther away the extrapolation the larger the uncertainty. The chosen sequence still allows to compare with data for more than half of the sample. The actual deviations from available experimental values (shown as filled circles) are significantly larger than the estimates of uncertainty from statistical analysis. The fig-

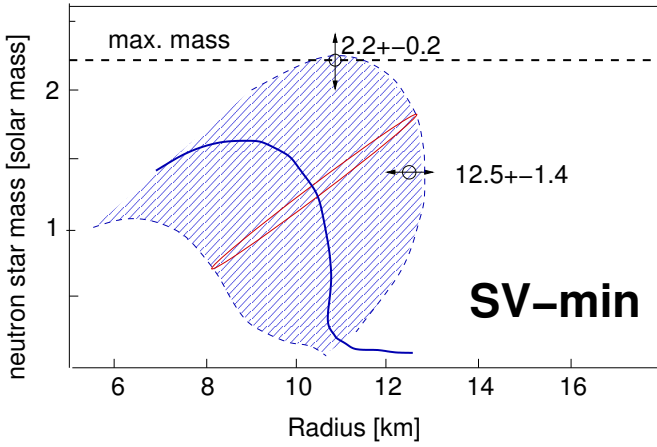


Fig. 3: Mass-radius relation of a neutron star computed for SV-min (heavy blue line). The shaded area indicates the range of the extrapolation errors. The mass-radius correlation ellipsoid is shown by a red line. The dashed horizontal line indicates the mass of the heaviest identified neutron star. The black dots with errors stand for the maximum mass and maximum radius from SV-min. Data taken from [96].

ure demonstrates nicely the possible devastating effect of a systematic error. In this case we are in the lucky situation that we could already identify the problem because there are sufficient data for checking, see figure 1 and the discussion thereof. The case becomes uncontrollable for totally new observables for which one does not dispose of benchmark data. Nonetheless, with the statistical extrapolation error we have an indispensable tool to get an idea about the uncertainties to expect and a safe lower estimate for them. Mind the the extrapolation uncertainty in figure 2 has at least the correct order of magnitude.

Figure 3 addresses as next example the extrapolation to neutron star mass and radii. The heavy line shows the results of the Tolman-Oppenheimer-Volkov equation for the mass-radius relation using as input the neutron equation-of-state from SV-min [96]. The faint horizontal line indicates the maximum mass of a neutron star found so far [97]. This sets a lower limit for the maximal mass because one cannot exclude that an even heavier star may be found some day. The prediction from SV-min stops far below the wanted maximum mass. However, the outlook improves when taking into account the extrapolation errors, marked by the shaded area. The uncertainties are huge which is understandable because we deal here with a really far extrapolation, from finite nuclei to comparatively infinite star matter. The good news is that the error band scratches the wanted maximum mass. This indicates that inclusion of wanted neutron star properties can be accommodated by a  $\chi^2$  fit without sacrifices. This was done with success in [96] yielding the parametrization TOV which indeed hits correctly the mass line and has also a much smaller uncertainty band due to the inclusion of star data. The figure 3 contains one more detail. This is the error ellipsoid plotted inside the error band. It indicates the region in which the probability distribution (30) is larger than  $1/2$ , this is the region of predictions from the range of “reasonable parametrizations”. In this example, the ellipsoid looks more like a needle going diagonal through the error band. This means that we encounter

here a highly correlated scenario where a given value of radius fixes inevitably a corresponding value for mass. It is a prototype example for a case with large covariance (32d) close to 1.

### 6.1. Hierarchy of terms in the functional

The SHF functional (6) was motivated by a Taylor expansion of the a supposed microscopic effective interaction, see section 2.3. This implies a hierarchy of importance of the terms in the functional with the zeroth order of expansion (the purely density dependent parts) representing the leading terms. A further ordering principle comes from the fit data. The landscape of known nuclei extends widely over size  $A$  but only over a narrow band of isotopic chains. This means that isoscalar properties are well determined by the long trends with  $A$  while knowledge of isovector properties is limited by the small extension in isovector direction  $N - Z$  together with the fact that only one sort of density is well known empirically, namely the proton density measured by electron scattering [57]. This combined sorting principles led to the assignment of a “minimal set of terms” as indicated by yellow (gray) shading in eq. (6). In this section, we are going to explore the importance of terms in detail by starting from the most sparse model using only density dependent terms and adding step by step more terms up to the full model (6). At each stage, the model consisting out of the chosen terms is optimized by minimization of  $\chi^2$  always using the same data pool from [32], see end of section 4.1 and appendix B. This tries to make the best out of the given functional. The strategy differs from a similar investigation of stages in [39]. There, we started from ab-initio calculations in bulk matter to define the background of LDA similar as in electron systems [22] and added stepwise derivative terms with information on finite nuclei. Here we optimize each stage as far as possible.

We consider the following stages of the model:

LDA:

This first stage invokes the terms with the parameters  $C_0^\rho$ ,  $C_1^\rho$ ,  $C_0^{\rho,\alpha}$ , and  $\alpha$ . It covers only the purely density dependent terms which are active in homogeneous matter. We call it LDA because that choice produces a purely density dependent functional (no derivative terms wherever). But we optimize it empirically. It is not LDA in its strict sense where exact solution for bulk matter are used to deduce a functional [22].

+grad:

To the previous stage, the term  $\propto C_0^{\Delta\rho}$  is added. This gives the model the flexibility to account for surface properties.

+ls:

To the previous stage, the isoscalar spin-orbit  $C_0^{\nabla J}$  term is added. This allows to put shell closures at the right place.

+ $C_1^{\rho,\alpha}$ :

To the previous stage, the density dependent isovector term  $\propto C_1^{\rho,\alpha}$  is added. This allows to resolve more isovector trends in the ground state properties, if there are still any.

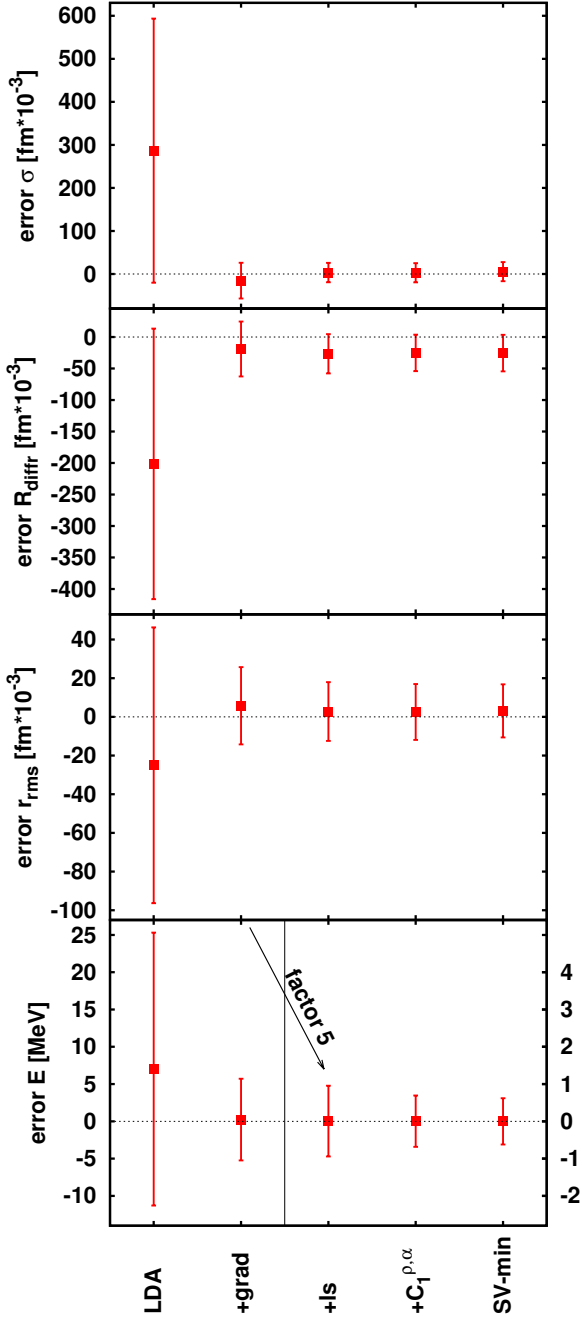


Fig. 4: Average and r.m.s. errors on basic bulk properties, binding energy  $E_B$ , charge r.m.s. radius  $r_{\text{rms}}$ , charge diffraction radius  $R_{\text{diff}}$ , and charge surface thickness  $\sigma_{\text{surf}}$ . Averages are taken over the pool of fit nuclei. The average deviation from data is shown by filled boxes and the r.m.s. deviation by the error bars around the boxes. Results are shown for the series of fits with increasing number of terms in the functional (6), see text. The lower panel for errors on binding energy is split into two energy scales. The first two entries (“LDA” and “+grad”) are plotted with respect to the scale on the left y-axis, the other three with respect to the right y-axis which is stretched by factor 5 with respect to the left scale.

SV-min:

This is result from invoking the full SHF functional (6). It was published in [32] and discussed in great detail there.

In all cases, we include, of course, the pairing functional (8). The first two stages (“LDA” and “+grad”) are too rough to deserve a detailed pairing adjustment. Here we use volume pairing, i.e.  $\rho_{0,\text{pair}} \rightarrow \infty$ , with fixed  $V_{\text{pair},p} = V_{\text{pair},n} = 300 \text{ MeV fm}^3$ . For the further three stages which provide a detailed modeling, we optimize all three pairing parameters together with the free parameters of the SHF model.

Figure 4 shows for the above listed sequence of stages of the model average and r.m.s. deviations for the four fitted bulk properties where averages are taken over the pool of fit data. The errors for the simplest stage, LDA, are large, particularly for the binding energy where the error band reaches  $\pm 20 \text{ MeV}$ . But this is, in fact, a satisfying result. It shows that already these few leading terms are capable of accommodating roughly the energies over all  $A$ , and even better for radii and surface thickness. Of course, details are bound to be wrong because we are yet missing the spin-orbit term and thus put shell closures at the wrong nucleon numbers.

Adding the gradient term allows to tune the nuclear surface energy. This improves the average quality of energy by half an order of magnitude. With  $\pm 4 \text{ MeV}$  it is as far as one can come without appropriate shell effects. The description is even better for radii and surface thickness because shell fluctuations play a minor role in these observables. Here one has reached almost the final quality. The great improvement due to the gradient term shows that the surface energy is a crucial contribution to a nuclear energy functional. This complies with the same findings in the purely macroscopic droplet model of the nucleus [52, 53].

The next substantial improvement is achieved with adding the spin-orbit force, stage “+ls”. This yields a mean-field model where shell closures emerge at the right nucleon number and also all other shell effects acquire the correct place and magnitude. Consequently, we see another dramatic reduction of the energy error. The model has now reached a high quality. All further terms deliver only gradual improvement. The stage “+ls” with its 6 free SHF parameters thus represents a minimal model which produces already an excellent description of the fit observables (bulk properties of the nuclear ground states).

In the step to stage “+C<sub>1</sub> <sup>$\rho, \alpha$</sup> ”, we explore the gain by adding more isovector flexibility. There is minimal improvement in the quality of radii and surface thickness and there is a 25% reduction in the energy error, not dramatic but non-negligible either. There is thus sufficient isovector information in the fit pool to fix this second isovector parameter.

Finally with “SV-min”, we have activated all terms in the functional (6). The gain as compared to the previous stage is extremely small. The additional terms in that step are all of isovector type and the pool of fit data does not contain enough isovector information to fix them. Thus “SV-min” leaves large uncertainties in these isovector parameters. Further data are required to determine the isovector model parameters more precisely. Isovec-

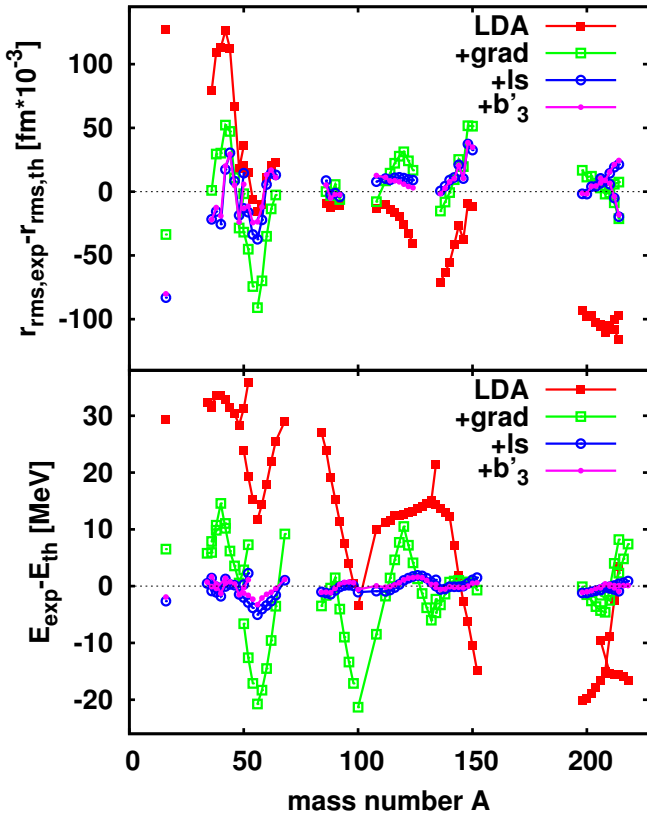


Fig. 5: Trends of deviations from data for the series of fits with increasing number of terms in the functional, see section 2. The lower panel shows deviations for the binding energy  $E_B$  and the upper panel for the charge r.m.s. radius  $r_{rms}$ . Results along isotopic or isotonic chains are connected by a line.

tor response properties (GDR, dipole polarizability, and NMP, see section 6.3) and the neutron skin (21) add valuable information as we will see later.

Figure 5 shows the detailed map of deviations from data for the above introduced stages of the SHF functional. For simplicity, the plot is limited to errors in energy and r.m.s. radius. The diffraction radius and surface thickness behave similar. The errors for LDA show a strong trend over mass number  $A$ . The fit for LDA has found a global compromise between light and heavy nuclei. But the model at LDA level is not capable to deal properly with system size. The step to “+grad” resolves the global trend at once. A straight line through the errors is identical with the zero line. But there remain the strong shell fluctuations which are due to the fact that shell closure lie at the wrong nucleon numbers. These fluctuations are much reduced with the step to “+ls” whose energy errors (lower panel) then gather closely around the zero line. The errors on radii (upper panel) seem to be more resistive. But this impression is to a large extend a matter of scale. LDA delivered already quite good values for the radii. In turn, the discrepancy between LDA and further stages is not as dramatic for the radii as it is for energy (see also figure 4). Thus we see the deviations on radii with higher resolution and that reveals more clearly the irresistible unresolved trends.

The further steps deliver only gradual improvement, hardly distinguishable at the scales of this plot. The remaining errors, however, are still not statistically dis-

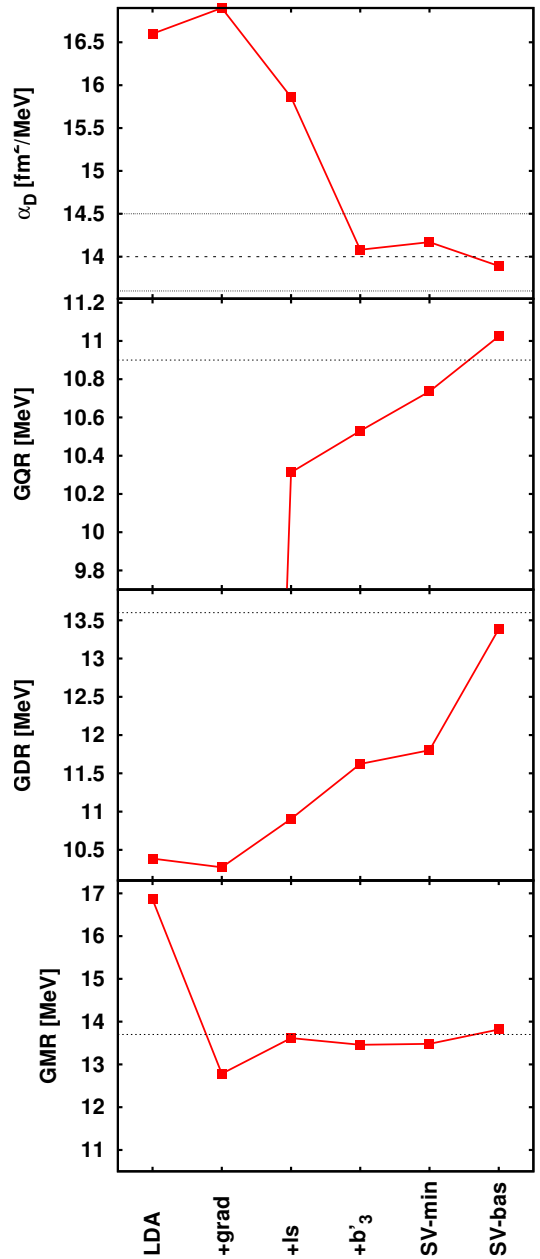


Fig. 6: Predictions for giant resonances and dipole polarizability in  $^{208}\text{Pb}$  compared with experimental data. Results are shown for the series of fits with increasing number of terms in the functional. A new entry as compared to figure 4 and 5 is the parametrization SV-bas. It is fitted the same way as SV-min but includes constraint an NMP in order to allow also a good reproduction of giant resonance energies, see [32].

tributed. There remain some unresolved trends seemingly related to shell structure (shell closures versus mid shell). This calls for further refinement of the model. But it is yet open whether this can be achieved within the SHF and pairing functional or whether we are forced to invoke correlation effects.

Figure 6 shows the peak energies for giant resonances and the dipole polarizability for the stages of the SHF functional, all for the nucleus  $^{208}\text{Pb}$ . The lower panel shows the GMR. It improves with each stage and reaches already at the minimal model, stage “+ls”, good agreement with the experimental value. This is not surprising. The GMR is closely tied to the incompressibility



$K$  which characterizes the response to changes in density [98, 99]. The incompressibility, in turn, depends on the parametrization of density dependence in the model. And this seems to be well determined by the fit data which span a broad range of mass numbers (isoscalar information). We learn that the isoscalar aspects are already well converged with the stage “+ls”.

The second panel from below shows results for the GDR. They are all far below the experimental point even. The reason is clear for all stages before SV-min because these do not invoke the effective mass terms  $C_T^\tau$  and it is known that the GDR depends sensitively on TRK sum-rule enhancement  $\kappa_{\text{TRK}}$  which is closely related to  $C_1^\tau$  [100, 32]. But even the step to for SV-min, which includes all terms of the functional does not improve the situation. The fit data are not strict enough to push  $\kappa_{\text{TRK}}$  to the right value. On the other hand, they do not fix  $\kappa_{\text{TRK}}$  so much. The uncertainty in the GDR energy is 1.4 MeV for SV-min. This leaves sufficient leeway to tune  $\kappa_{\text{TRK}}$ . This is done with the parametrization SV-bas which optimizes some NMP to tune the giant resonances in  $^{208}\text{Pb}$ [32]. This leads obviously to a good reproduction of the GDR.

A similar situation is encountered for the GQR (second panel from above). All stages up to including SV-min underestimate its resonance energy. This is no surprise for the stages LDA through “ $+C_1^{\rho,\alpha}$ ” because they do not invoke the term  $\propto C_0^\tau$  and thus have a mean field with effective mass  $m^*/m = 1$ . But the GQR is known to depend sensitively on  $m^*/m = 1$  and require a lower value 0.8–0.9 [101]. This option is set free with SV-min. Similar as for the GDR, SV-min does not put  $m^*/m$ , and with it the GQR, at the right place, but leaves sufficient leeway to tune it properly. This is again achieved by SV-bas.

The upper panel in figure 6 shows the dipole polarizability  $\alpha_D$  for the various stages of the functional. It starts for LDA with a rather wrong value, improves with each step, and reaches the data already at the stage “ $+C_1^{\rho,\alpha}$ ” where the functional was given sufficient isovector freedom to take advantage of the (static) isovector information in the fit data.

It is interesting to note that two data points, GMR (related to incompressibility  $K$ ) and  $\alpha_D$ , are well described already from the fits to ground state data while the two other, GDR and GQR, need extra measures. Mind that  $K$  and  $\alpha_D$  are static response properties. No surprise then that they are well determined by ground state data. The GDR and GQR, on the other hand, are related to the dynamic response properties  $m^*/m$  and  $\kappa_{\text{TRK}}$ . It is plausible that dynamical properties require dynamic data for calibration. Thus we need some information from excited states to fully fix the functional (6).

## 6.2. Impact of groups of data

In this section, we take up point 3.3 of the analyzing strategies outlined in section 5, the variation of fit data. An analysis following this strategy was already given in [94]. We repeat part of that material for a reduced set of variations and, on the other hand, add new variations. Basis is the pool of fit data as developed in [32], see also end of section 4.1 and appendix B. An unconstrained fit to the full set yields the parametrization SV-min. Now we are

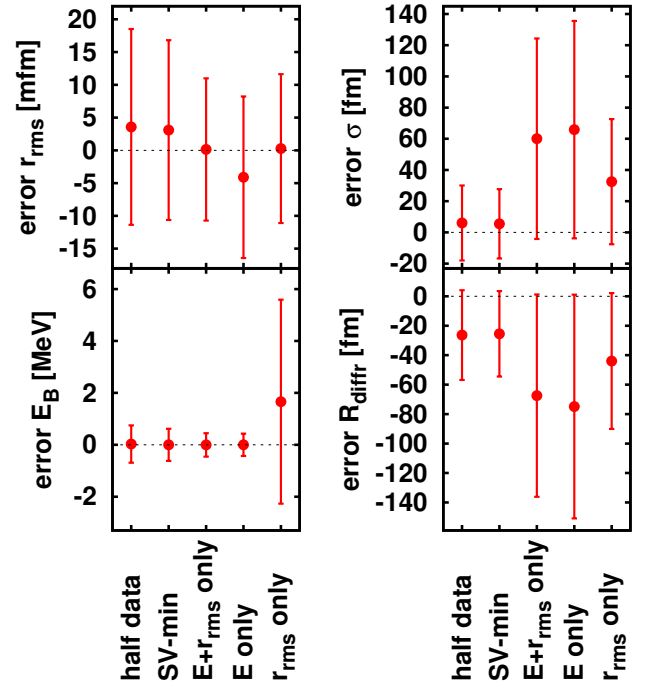


Fig. 7: Average and r.m.s. errors on basic bulk properties, binding energy  $E_B$ , charge r.m.s. radius  $r_{\text{rms}}$ , charge diffraction radius  $R_{\text{diff}}$ , and charge surface thickness  $\sigma_{\text{surf}}$ . Averages are taken over the pool of fit nuclei. The average deviation from data is shown by filled boxes and the r.m.s. deviation by the error bars around the boxes. Results are shown for the series of fits with different selections of groups of data as listed in table 2.

interested in fits with deliberate omission of groups of fit data. This yields the parametrizations as listed in table 2.

	$E_B$	$r_{\text{rms},C}$	$R_{\text{diff},C}$	$\sigma_C$
“half data”	x/2	x/2	x/2	x/2
SV-min	x	x	x	x
“ $E+r_{\text{rms}}$ only”	x	x	-	-
“ $E$ only”	x	-	-	-
“ $r_{\text{rms}}$ only”	-	x	-	-

Table 2: Included data sets from the standard pool of fit data from finite nuclei [32]. A “x” means included, “-” stands for excluded, and “x/2” means that only half of the data were included. Pairing gaps  $\Delta_{\text{pair}}$  and spin-orbit splitting  $\varepsilon_{\text{ls}}$  are included in all data sets and not listed explicitly above. The observables were explained in section 3.2.

We have also studied omission of  $\varepsilon_{\text{ls}}$  or  $\Delta_{\text{pair}}$ . This showed only minor effects and will be not reported here.

Figure 7 demonstrates the effect of varied fit data on the average and r.m.s. residuals taken separately over a group of data. Mean values deviating significantly from zero within the scale set by the uncertainties indicate some basic incompatibility of the observable with the model. Changes on the r.m.s. error indicate the sensitivity to a group of observables.

First, we should realize that the scales in this figure are generally much smaller than those of the various stages of the functional in figure 4. All fits with reduced data sets

produce very similar models. Even when taking “ $E$  only” or even “ $r_{\text{rms}}$  only” we obtain an agreeable model. This gives us some confidence that the model has predictive power and allows extrapolations to other observables or other regions of nuclei.

However, looking closer at the results in figure 7 we see at some places differences which carry some information on tensions within the model and at other places continued similarity which indicates the strongholds of the model.

Let us first compare the set “half data” with SV-min. Both sets produce exactly the same averages. In fact, looking at detailed residuals (not shown here) we find that both fits produce very similar results. This can be read off also globally from the fact that the r.m.s. errors (taken over all data) are similar. This proves that the SHF functional interpolates well.

The step from SV-min to “ $E+r_{\text{rms}}$  only” has dramatic consequences for  $R_{\text{diff},C}$  and  $\sigma_C$ . The average error in these two observables makes a large jump upward and similarly the r.m.s. error. This indicates that there is some incompatibility between  $r_{\text{rms},C}$  and  $R_{\text{diff},C}$  in the present model. That could already be spotted in SV-min. Already here, we find a large average error for  $R_{\text{diff},C}$ . In fact, the r.m.s. error is almost exhausted by the average error. The same behavior persists in the step to “ $E$  only”. But here, we also find the same increase in the average error for  $r_{\text{rms},C}$  which indicates a slight incompatibility of  $E_B$  and  $r_{\text{rms},C}$ . It is likely that both incompatibilities, for  $R_{\text{diff},C}$  as well as for  $r_{\text{rms},C}$  are related to insufficiencies in the surface profile and thus to the model of density dependence.

The average error of energy  $E_B$  is near zero for all fits which include  $E_B$ . This indicates that the SHF functional is well suited to adjust the energy over all ranges of nuclei. The model “ $r_{\text{rms}}$  only” produces a slight mismatch of the average. However, these stay well within the huge error bars in this case. The large size of the error bars can be viewed as an “automatic” warning from the  $\chi^2$  analysis. It signals that the data set “ $r_{\text{rms}}$  only” does not contain sufficient information to fix the energies. It is remarkable, though, that the other direction, determining  $r_{\text{rms}}$  by a fit “ $E$  only”, works much better. Energies are the leading input to the pool of fit data.

Figure 8 shows the effect of varied fit data on predicted/extrapolated observables, nuclear matter properties (NMP) and key observables of the three nuclei  $^{208}\text{Pb}$ ,  $^{266}\text{Hs}$  and  $Z=120/N=182$ . For  $Z=120/N=182$ , we consider binding energy  $E_B$  and  $\alpha$ -decay energy  $Q_\alpha$  according to eq. (20). No data are available yet for this nucleus. For  $^{266}\text{Hs}$ , we consider binding energy  $E_B$  [102] and fission barrier  $B_f$  [103]. The experimental value for  $B_f$  is given with error bar as it is associated still with large uncertainty. The binding energy includes the rotational zero-point energy (12) which is obligatory for deformed nuclei. In  $^{208}\text{Pb}$ , we consider response properties, the peak energies of GMR, GDR, and GQR and the dipole polarizability  $\alpha_D$  (see section 3.2). The NMP considered are: binding energy  $E/A$ , density  $\rho_{\text{nm}}$ , incompressibility  $K$ , isoscalar effective mass  $m^*/m$ , symmetry energy  $a_{\text{sym}}$ , and Thomas-Reiche-Kuhn (TRK) sum rule enhancement factor  $\kappa_{\text{TRK}}$ , all taken at the equilibrium point of symmetric matter. Figure 8 shows the effect of variation of fit

data on the observables and their uncertainties. Changes in uncertainty indicate the importance of the omitted data group on the observable. A shift of the average shows what data are pulling in which direction.

The effects on NMP (left two columns) are generally large. A most pronounced shift is produced by omitting the formfactor information of  $R_{\text{diff},C}$  and  $\sigma_C$  in “ $E+r_{\text{rms}}$  only” and “ $E$  only”. This leads to a large jump in bulk equilibrium density  $\rho_{\text{nm}}$  and incompressibility  $K$ . There is also a jump in the isovector response  $a_{\text{sym}}$  in addition to the generally strong changes. It is also interesting to note that formfactor information keeps the effective mass  $m^*/m$  down to values below 1 while fits without radii let  $m^*/m$  grow visibly above one. The reason is probably that  $m^*/m$  has an impact on the surface profile, thus on  $r_{\text{rms},C}$  and  $\sigma_C$ , and, in turn, also on  $R_{\text{diff},C}$ . This suggests that the formfactor is closely related to the surface profile of the nucleus. This, in turn, seems to be connected with modeling the density dependence as one can read off from the strong impact on  $K$  (second derivative with respect to density). The step to “ $r_{\text{rms}}$  only” restores approximately the values of  $\rho_{\text{nm}}$  and  $K$  from the full fit SV-min. This indicates that there is also some competition between  $r_{\text{rms}}$  and  $E_B$ . These two quantities pull in different direction which indicates that they would prefer different surface profiles. Mind, however, that the deviations in the average errors are fully compatible within the error bars (characterizing the r.m.s. errors). This means that all choices of subsets of data are compatible when taking into account the message about uncertainties of a fit which is quite appropriately delivered by statistical analysis. Nonetheless, the observed variations of average errors indicate that the SHF functional may deserve further fine tuning to reduce these conflicts between observables. The most likely aspect to work on is the density dependence of the functional.

The variances usually grow when omitting data which is plausible because less data mean less determination. Particularly large errors emerge for the sets “ $E$  only” and “ $r_{\text{rms}}$  only”. This shows that combined information with the charge formfactor is extremely useful to confine the parametrization. But mind that the error bars for “ $E$  only”, although being generally larger, are still in acceptable ranges. This shows that data from energy alone can already provide a reasonable parametrization. One may argue similarly with the errors for “ $r_{\text{rms}}$  only”. But here the error on  $E/A$  is rather large which was already foreseeable from the also large error on energies of finite nuclei seen in 7. Besides  $E/A$ , the parametrization “ $r_{\text{rms}}$  only” yields also a very large error on the symmetry energy  $J$ . This happens because the selection of nuclei with radius data is smaller along isotopic chains thus carrying even less isovector information.

Column 3 of figure 8 shows the effect of variation of fit data on response observables in  $^{208}\text{Pb}$ . The three giant resonances and the polarizability  $\alpha_D$  are known to have a one-to-one correspondence with each one NMP (see sections 6.3, 6.5, and ref. [32]): the GMR with  $K$ , the GQR with  $m^*/m$ , the GDR with  $\kappa_{\text{TRK}}$ , and  $\alpha_D$  with  $a_{\text{sym}}$ . These pairs of highly correlated observables show exactly the same trends in the figure which confirms the correspondence also from this point of view. Unlike NMP,



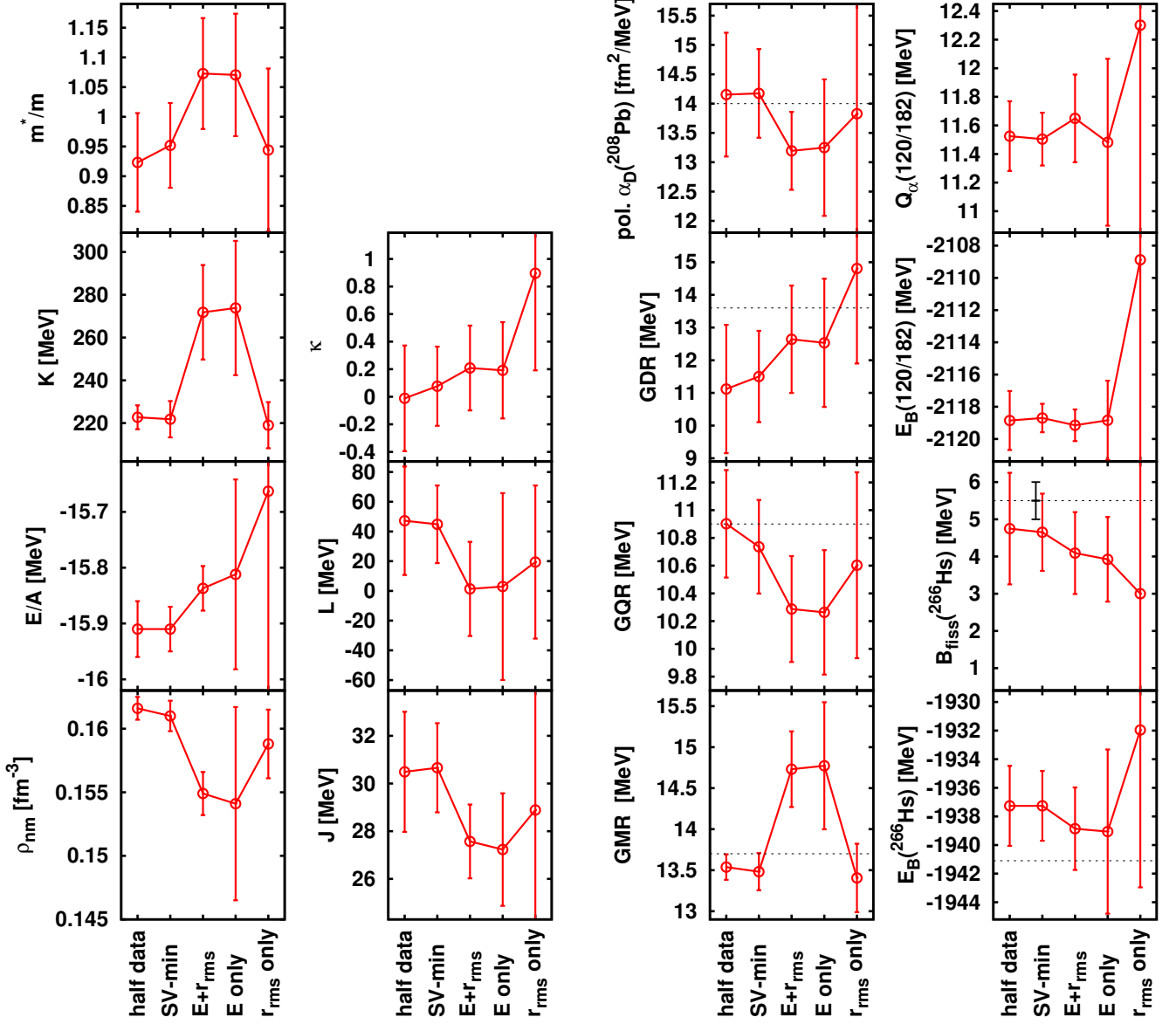


*Fig. 8:* Results on NMP (left two columns) and specific observables in finite nuclei (right two columns) for the three fits to different data sets: “SV-min” = fit to the full standard data pool of [32], “ $E + r_{\text{rms}}$  only” = energies and r.m.s. radii in the pool plus gaps and l\*s splittings, “ $E$  only” = energies in the pool plus gaps and l\*s splittings. Left column: isoscalar NMP. Second from left column: isovector NMP. Third column: Giant resonance energies and polarizability in  $^{208}\text{Pb}$ . Right column: binding energy and fission barrier in  $^{266}\text{Hs}$  and binding energy and  $\alpha$ -decay energy in the the hypothetical super-heavy nucleus  $Z=120/N=182$ .

observables in finite nuclei allow a comparison with experimental data. GMR and  $\alpha_D$  are related to the static response properties  $K$  and  $J$ . Comparison with data shows clearly that inclusion of formfactor information drives into the right direction while a fit without  $R_{\text{diff},C}$  and  $\sigma_C$  yields less favorable values. This indicates that information from the formfactor carries correct physics about the nuclear response although these data were found in the previous figure to stay slightly in conflict with energy information. The situation is mixed for the dynamical response properties. The GDR improves with omitting  $R_{\text{diff},C}$  and  $\sigma_C$  while GQR deteriorates this way. This is very likely pure chance because dynamic response is not embodied in ground state data. An explicit fit of dynamic response, as done e.g. in SV-bas [32], is anyway recommended.

The situation is mixed for the super-heavy elements (SHE) shown in column 4 of figure 8. As several times before, all predictions agree with each other within their error bars. There remains to comment a few trends of average values. Skipping  $R_{\text{diff},C}$  and  $\sigma_C$  (parametrization “ $E+r_{\text{rms}}$  only”) improves  $E_B(^{266}\text{Hs})$  but spoils  $B_f(^{266}\text{Hs})$ . Skipping, furthermore  $r_{\text{rms},C}$  to parametrization “ $E$  only” does not make much of further changes. However, the parametrization “ $r_{\text{rms}}$  only” spoils both  $E_B(^{266}\text{Hs})$  and  $B_f(^{266}\text{Hs})$ . There are even less trends in the averages for the SHE  $Z=120/N=182$ , except for “ $r_{\text{rms}}$  only” which is obviously totally inappropriate for SHE. This is also signaled by huge error bars which “ $r_{\text{rms}}$  only” produces in all four observables of SHE. The data basis of r.m.s. radii is obviously too weak to allow for far extrapolations. The examples demonstrate that statistical analysis combined with variation of model or conditions delivers very useful insight into the model.

### 6.3. Systematic variation of nuclear matter properties (NMP)

In this section, we exemplify the strategy 3.2 (see section 5), namely systematic variation of a model parameter or property. We have argued in section 3.1 that the NMP as defined in table 1 are fully equivalent to the parameters of the SHF functional and have the additional advantage that they carry an intuitive physical meaning. We follow here the strategy of [32] and define a base point with the following four NMP fixed:  $K = 234$  MeV,  $m^*/m = 0.9$ ,  $J = 30$  MeV, and  $\kappa_{\text{TRK}} = 0.4$ . These values were chosen because they lead to a good reproduction of the four basic response properties in  $^{208}\text{Pb}$ : GMR, GDR, GQR, and  $\alpha_D$ . A fit with these four NMP fixed delivers the parametrization SV-bas. Starting from this base point, we have produced four chains of parametrizations where one of the NMP was varied systematically while the other three were kept fixed. A detailed description of this set of parametrizations is given in [32]. In the following we use this set for the examples.

Figure 9 shows the trends of the four crucial response properties in  $^{208}\text{Pb}$  with the four NMP. The lower left panel shows the variation with  $K$ . Only the GMR moves with  $K$  while the other three response properties react only weakly. This makes it obvious that the GMR is uniquely related to  $K$ . The upper left panel demonstrates in the same way the close relation between GQR and

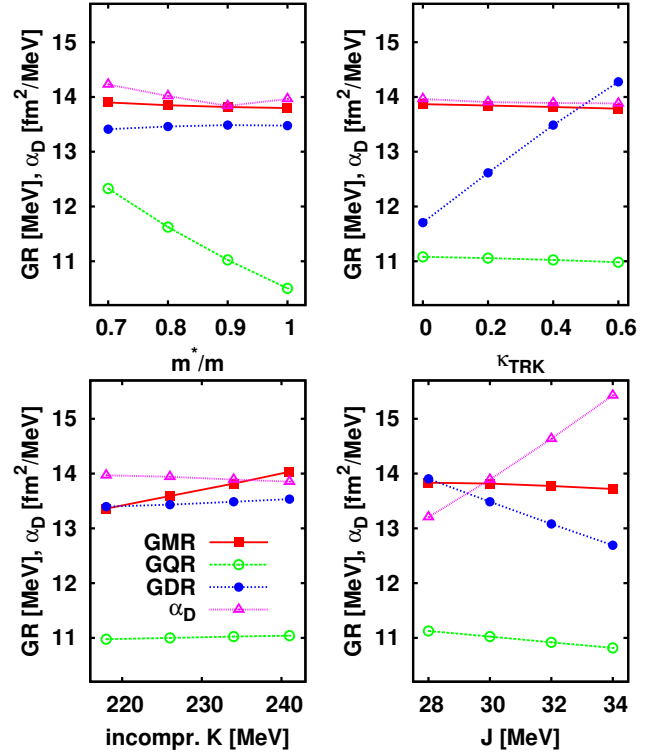


Fig. 9: Peak energies of giant resonances (GMR, GDR, GQR) and dipole polarizability  $\alpha_D$  in  $^{208}\text{Pb}$  for sets of parametrizations with systematically varied NMP from [32] as indicated on the  $x$ -axes.

$m^*/m$ . And similarly, we see the unique relation between GDR and  $\kappa_{\text{TRK}}$  in the upper right panel. The lower right panel shows the trends with  $J$ . Here it is the dipole polarizability  $\alpha_D(^{208}\text{Pb})$  which shows the strongest dependence. There is some trend for the GDR, but this remains smaller than the trend for  $\alpha_D$  versus  $J$  or for the GDR’s dependence on  $\kappa_{\text{TRK}}$ . Thus we conclude from these four variations that there is a one-to-one relation between the four response properties and the four varied NMP. These findings are confirmed even more clearly by correlation analysis in section 6.5 and figure 14 therein.

One may wonder why a variation of  $L$ , the slope of symmetry energy, is not considered. The point is that  $J$  and  $L$  are highly correlated with each other (covariance near 1) for the present SHF functional and pool of fit data. Thus a plot versus  $L$  shows the same trends as a plot versus  $J$ . This feature may change for extended SHF functionals which deliver more flexibility in the isovector part of density dependence. An example in that direction is the extension (35) which indeed reduces the correlation between  $J$  and  $L$  as will be seen later in the middle panel of figure 14.

Figure 10 shows the trends of fission barrier  $B_f$  and fission lifetime  $\tau_f$  of  $^{266}\text{Hs}$  (for its definition see section 3.2) for varied NMP. The dominant influence comes here from  $m^*/m$ . This is not surprising because fission is driven by shell effects and these are highly sensitive to  $m^*/m$ . The figure is, however, to some extent misleading. It gives the impression that fission is exclusively related to  $m^*/m$ . This view is not confirmed by correlation analysis [75, 94] where the covariance of  $B_f$  with  $m^*/m$  is about 0.2 which is some correlation but not a dominant one. The reason

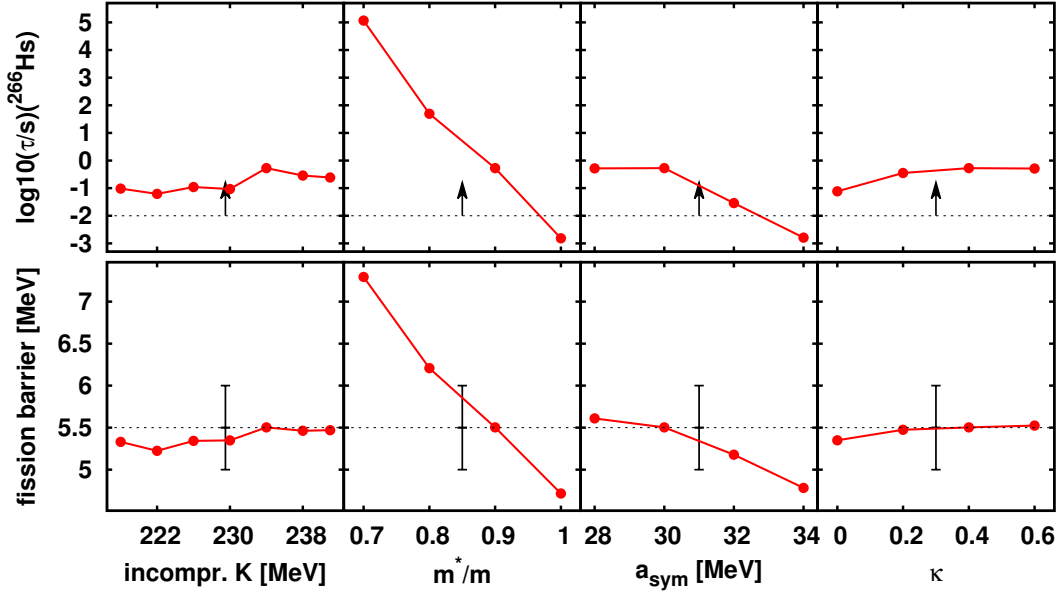


Fig. 10: Fission barrier  $B_f$  in  $^{266}\text{Hs}$  (lower panels) and fission half-life  $\tau_f$  (upper panels) for sets of parametrizations with systematically varied NMP as indicated on the  $x$ -axes.

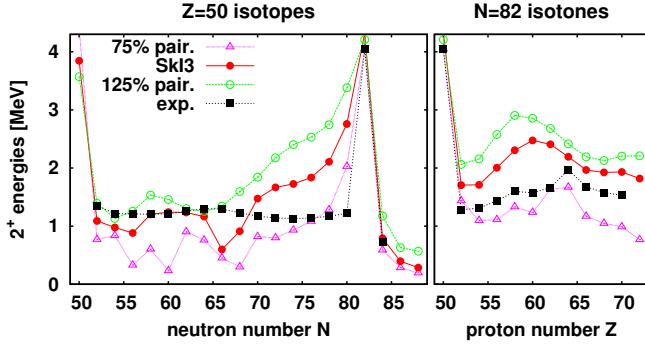


Fig. 11: Energy of the low-lying  $2^+$  state in the isotopic chain of Sn ( $Z=50$ ) and the isotonic chain with  $N=82$ . Shown are results for SkI3 [104] and a variation of pairing strength while keeping the SHF parameters of SkI3 fixed. Data taken from [41].

that there are several other agents which all have some impact on the fission path. The next larger influences come from the surface energy, spin-orbit term (also acting through shell effects), and pairing. The example demonstrates that systematic variation of force parameters is very instructive to reveal influences, but should be augmented by correlation analysis (section 6.5 and point 2.2 in section 5) to avoid premature conclusions.

Figure 11 shows the  $E_{2^+}$  energies of low-lying quadrupole states in the chain of even Sn isotopes and even  $N=82$  isotones. We show here the effect of a variation of pairing strength on the results. Similar as for the fission path, the collective path for large amplitude quadrupole vibrations is most strongly influenced by pairing and grabs a piece of influence from many other ingredients. Thus we show here only the strongest effect and refer the reader to [41] for the many more subtle variations. First, we point out that SkI3 with standard pairing provides satisfying results, particularly for Sn in the mid shell region. We see again that the SHF functional is capable to describe at once also large amplitude motion without having

been particularly fitted for that. Larger deviations occur near shell closures that is the region where collectivity is not so large such that the mapping of the collective path by a mere quadrupole constraint becomes insufficient [41]. One should employ here variationally optimized paths as delivered by adiabatic TDHF, see e.g. [46]. The effect of varied pairing is dramatic showing that low-lying  $2^+$  states are a sensitive probe for the pairing functional. This is a feature which has not yet been fully exploited in calibration strategies. The effect is particularly dramatic for the case of reduced pairing (purple line with filled triangles). The excitation energies shrinks occasionally to near zero. These are cases where pairing breaks down and it shows that the standard values of pairing strength are rather weak (i.e. close to the break-down regime).

#### 6.4. Impact of ab-initio data

The nuclear many-body problem is much more involved than the electronic one. The microscopic nucleon-nucleon interaction has a huge repulsive core at short distances and yet one cannot ignore long-range correlations from zero-sound modes. Moreover, it is not even correct to speak of a nucleon-nucleon interaction because nucleons are composite particles from quarks and gluons, and these constitute a highly non-linear field theory. In spite of all these enormous complications, much progress has been made with nuclear ab-initio calculations during the last two decades [19, 20, 21]. Time is coming close that we can refer to ab-initio calculations in bulk matter, perhaps also in finite nuclei [105]. Earlier attempts to use that for calibration of mean-field models were promising, but not yet fully satisfying, see e.g. the study in [39] on the basis of relativistic Brueckner-Hartree-Fock data of [106]. Ab-initio calculations have still further improved since then. In particular, there is one point which seems to be well settled. This is neutron matter at very low densities. This stage is called a correlated Fermi gas (CFG). In the limit of low densities  $\rho$ , or Fermi momenta  $k_F$  respectively, the CFG energy can

be parametrized in terms of the neutron kinetic energy as

$$\frac{E}{N_{\text{neut}}}(k_f) = \xi \frac{E}{N_{\text{kin,neut}}}(k_f) \quad (33)$$

where  $\xi$  is, in principle, function of  $k_F$ . We are interested here in the limit  $k_F \rightarrow 0$  for which  $\xi$  becomes just one number. Many-body theory predicts a value  $\xi(0) = 0.38 - 0.44$  for the CFG [107, 108].

It is straightforward to compute  $\frac{E}{N_{\text{neut}}}$  for the SHF functional. With the constituents of the total energy (4), we can deduce  $\frac{E}{N_{\text{neut}}} = (\mathcal{E}_{\text{kin}} + \mathcal{E}_{\text{Sk}}) / \rho_0$  and thus

$$\xi = 1 + \frac{\mathcal{E}_{\text{Sk}}}{\mathcal{E}_{\text{kin}}} \quad (34)$$

To estimate  $\xi$  in the low-density limit, we recall  $k_F \propto \rho^{1/3}$  and discuss the limit in terms of  $\rho$  because the SHF functional (6) is given that way. The kinetic density in homogeneous matter becomes  $\mathcal{E}_{\text{kin}} \propto \tau \propto \rho^{5/3}$  [109]. The leading term in the SHF functional is the two-body contact interaction  $\propto \rho^2$ . The density dependent term behaves as  $\propto \rho^{2+\alpha}$ . Successful parametrizations require  $\alpha > 1$ . This term, therefore, vanishes faster than  $\rho^2$  in the limit  $\rho \rightarrow 0$  and can be neglected. The kinetic interaction term behaves as  $\rho\tau \propto \rho^{8/3}$  which, again, can be neglected. It remains  $\xi \propto 1 + \rho^2/\rho^{5/3} \rightarrow 1$  in the limit  $\rho \rightarrow 0$ . Thus we see in purely analytical manner that the standard SHF-functional (6) cannot meet at all the requirement  $\xi(0) \approx 0.42$ .

In order to allow for a description of  $\xi < 1$ , we extend the SHF functional by adding to  $\mathcal{E}_{\text{Sk}}$  another density dependent term

$$\mathcal{E}_{\text{Sk,dens3}} = \left[ C_0^{\rho,-1/3} \rho_0^2 + C_1^{\rho,-1/3} \rho_1^2 \right] \rho_0^{-1/3} \quad (35)$$

It has the form of the density dependent term in the functional (6) with  $\alpha = -1/3$ . Handled as additional term, it allows to maintain the quality of the standard ansatz while opening the chance to accommodate the CFG limit.

We have produced two new parametrizations with the extended functional, now including also the term (35). Starting point is here, again, SV-min, a fit to the standard pool of fit data. The first new set is “ $+C_T^{\rho,-1/3}$ ” and uses the same data as SV-min. The second new set “+CFG” adds to these data the CFG condition  $\xi(0) = 0.42$  as further data point.

Figure 12 shows the resulting average and r.m.s. errors for the basic blocks of observables. The averages stay at zero level throughout for  $E_B$  and vary somewhat for radii and surface thickness. The fit “ $+C_T^{\rho,-1/3}$ ” with more freedom in density dependence, yet without enforcing the CFG point, leads always to lower average and r.m.s. errors. This confirms the impression gained in previous section that the slight conflict between energy and formfactor calls for improved density dependence. However, the step to “+CFG” deteriorates again radii and surface thickness in the average approximately back to the status of SV-min. The freedom coming along with the new term has been fully exploited by the CFG point.

Figure 13 shows NMP and response properties in  $^{208}\text{Pb}$  for the parametrizations introduced in this section. There are marked changes in the results from the three

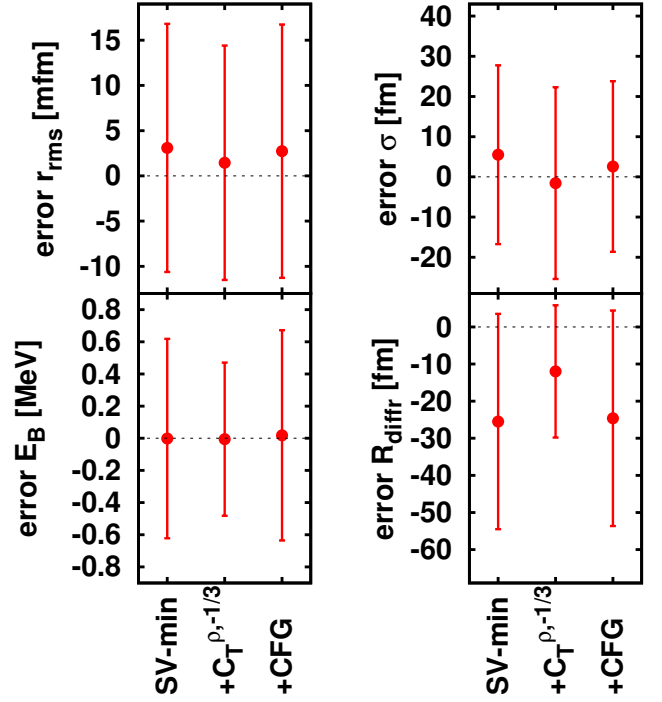


Fig. 12: Average and r.m.s. errors on basic bulk properties, binding energy  $E_B$ , charge r.m.s. radius  $r_{\text{rms}}$ , charge diffraction radius  $R_{\text{diff}}$ , and charge surface thickness  $\sigma_{\text{surf}}$  for the series of fits with the additional density dependent term (35) and four NMP fixed. Averages are taken over the pool of fit nuclei. The average deviation from data is shown by filled boxes and the r.m.s. deviation by the error bars around the boxes. The series is: “SV-min” = fit of standard functional to full data pool from [32]; “ $+C_T^{\rho,-1/3}$ ” = fit as SV-min but including the new term (35) in the functional; “+CFG” = fit as “ $+C_T^{\rho,-1/3}$ ” but including the CFG limit as data point.

parametrizations. But they are all compatible within the error bars. Nonetheless, it may be instructive to discuss the changes in the center values. Similar to the previous figure, we find that the results of SV-min and “+CFG” are closer together while “ $+C_T^{\rho,-1/3}$ ” makes generally the largest changes. Exceptions are the pair  $\kappa_{\text{GDR}}$  with GDR and  $K$  with GMR where “+CFG” produces too low values. The strong impact of the CFG point is plausible for  $K$  and GMR because these observables have direct relation to density dependence. The fact that the CFG point pulls the GMR away from the data indicates that the extended model is not yet ideal, although the data may be corrected by fitting with constraint on  $K$  in the manner as was done for SV-bas [32]. It is also noteworthy that the error bars for the free fit of the extended density dependence in “ $+C_T^{\rho,-1/3}$ ” produces particularly large uncertainties for  $K$  and GMR, the two observables sensitive to density dependence. This large uncertainty is much reduced by the step to “+CFG” which indicates once more that the CFG point has a strong impact on the density dependence of the model.

The example is also quite revealing as it shows that some long-range correlations (at least those at extremely low density) are not incorporated into the SHF functional. This is annoying because these correlations are smooth with mass number and thus should be contained in a

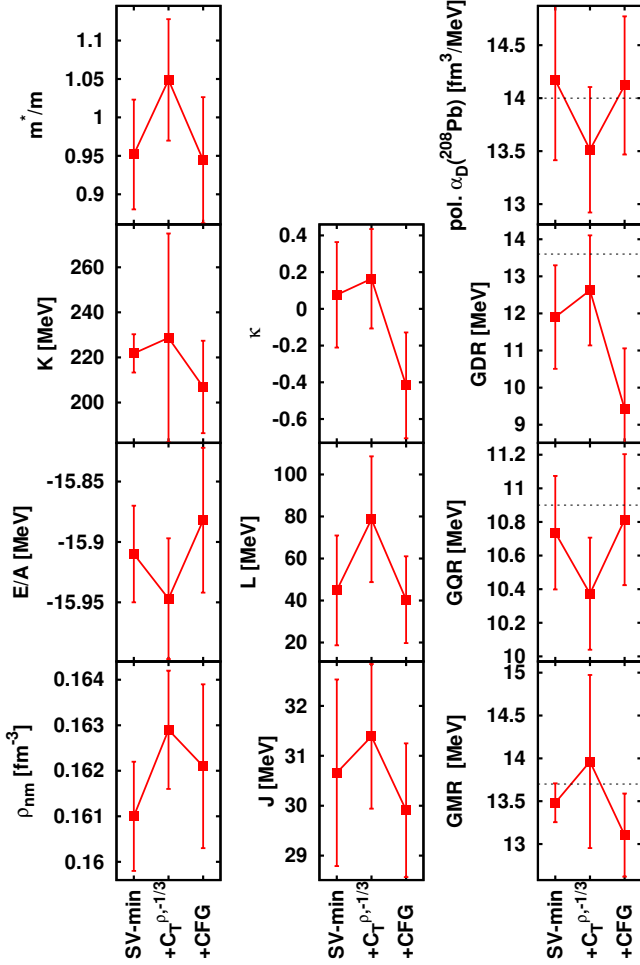


Fig. 13: Results on NMP (left two columns) and response properties of  $^{208}\text{Pb}$  (right column) for the series of three forces as in figure 12.

smooth functional. Again, we see that we need to improve on the density dependence of the SHF functional.

### 6.5. Correlation analysis

In section 4.2, correlations, or covariances respectively, between observables had been defined with eq. (32d). In this section we will give a few examples for a small, but relevant, selection of observables. The selection covers: the four NMP  $K$ ,  $m^*/m$ ,  $J$ ,  $\kappa_{\text{TRK}}$  together with the four related response properties in  $^{208}\text{Pb}$ , namely GMR, GDR, GQR, and  $\alpha_D$ ; for static isovector response we look also at  $L$ , neutron skin  $r_{\text{skin}}(^{208}\text{Pb})$ , and slope of the neutron equation of state  $\partial_\rho E/A_{\text{neut}}|_{\rho=0.1}$ ; finally we check extrapolations to exotic nuclei,  $E_B$  for the very neutron rich  $^{140}\text{Sn}$  and  $E_B$  as well as  $Q_\alpha$  for the super-heavy element  $Z=120/N=182$ . Three parametrizations will be considered: SV-min as the standard, “E only” from section 6.2 to exemplify the impact of the choice of fit data, and “ $+C_T^{\rho,-1/3}$ ” from section 6.4 to explore the impact of an extended functional.

Figure 14 shows the correlations between the selection of observables as indicated on the axes. As every observable can be related to any other, we show it as correlation matrix. Let us start with the parametrization SV-min, the

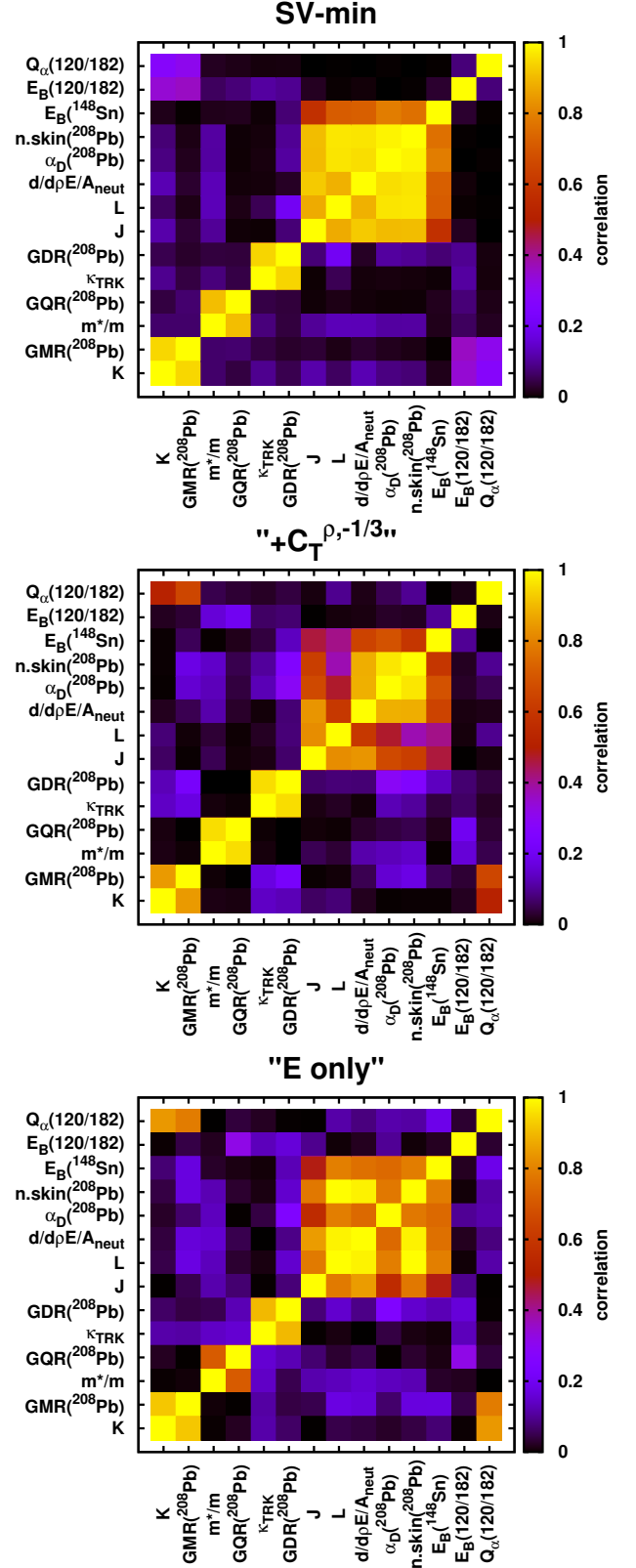


Fig. 14: Correlation matrix for a selection of observables as indicated. Three cases are shown: SV-min = fit of standard SHF functional to the standard pool of data from [32], “ $+C_T^{\rho,-1/3}$ ” = unconstrained fit as SV-min but with the functional extended by the density dependent term (35), “E only” = fit of standard functional to standard data pool without radii and surface thickness (see section 6.2).

straightforward fit to the standard pool of data [32]. We see clearly the strong correlation between  $K$  and GMR (static isoscalar response),  $m^*/m$  and GQR (dynamic isoscalar response),  $\kappa_{\text{TRK}}$  and GDR (dynamic isovector response), and for the whole group of static isovector response covering here the NMP  $J$ ,  $L$ ,  $d/d\rho E/A|_{\text{neut}}$  (see section 3.1) together with the finite nuclei observables  $\alpha_D$  and  $r_{\text{skin}}$  (labeled “n.skin” in the figure). For the exotic nuclei, there is some correlation of  $E_B(^{140}\text{Sn})$  to isovector static response which is plausible for a extremely neutron rich nucleus with very large isospin. The two data in the super-heavy element  $Z=120/N=182$  are nearly decoupled from the other groups of data. One may admit some correlation with  $K$  & GMR. This super-heavy region is dominated by shell effects and not so much by the bulk properties included in this correlation matrix. It is also interesting to remark that  $E_B$  and  $Q_\alpha$  are almost uncorrelated. Differences of energies often filter quite different aspects of a model than the energy as such.

We now look at the correlations produced by the next two parametrizations, with less data in “ $E$  only” and with more terms in the model in “ $+C_T^{\rho,-1/3}$ ”. In both cases, we see generally reduced correlations what we could have expected. It is, however, remarkable how small the reduction is leaving the gross structure of the correlations fully alive. There remain clearly the blocks for the four different responses. Larger changes are seen for isovector static block. And here, the changes are very different for the two different variations of the fit. For example, while “ $E$  only” degrades the correlations for  $J$  thus making  $L$  the leading bulk parameter for isovector static response, the other parametrization “ $+C_T^{\rho,-1/3}$ ” degrades just  $L$  and leaves  $J$  more intact. In such details, we see indeed a dependence on model and data pool. But recall that the general structure of correlations was robust.

There is another interesting detail concerning the super-heavy element  $Z=120/N=182$ . The independence of  $E_B$  and  $Q_\alpha$  persists. But there is now more correlation between  $Q_\alpha$  and  $K$  & GMR than was seen for SV-min. This shows that correlations are not necessarily reduced by less data or a large model. It can also happen that more freedom allows to explore connections which were hindered before by a too rigid model.

## 6.6. Spin sensitive applications: spin modes, odd nuclei, TDHF

This section is devoted to the spin properties of SHF. Spin properties are crucial for a broad range of applications. They play a role already for ground state properties, namely in case of odd nuclei, see e.g. [110, 111, 112, 113]. They are key players in spin excitation modes, see e.g. [114, 115, 116], they play a role in rotating nuclei, see e.g. [117, 118], and they can contribute to energetic heavy-ion collision described by time-dependent Hartree-Fock (TDHF) with the SHF functional, for an example where the impact of a spin excitation is discussed explicitly see [119]. Unfortunately, the spin terms are presently the least well controlled part of the SHF functional. Their proper calibration is yet an open problem and they are most prone to introduce instabilities into the SHF equations, for a crit-

$C_0^s$	$= -\frac{1}{3}(3C_1^\rho + 2C_0^\rho),$
$C_1^s$	$= -\frac{1}{3}C_0^\rho,$
$C_0^{\Delta s}$	$= -\frac{C_0^{\Delta\rho} - C_1^{\Delta\rho}}{2} + \frac{C_0^\tau - C_1^\tau}{8},$
$C_1^{\Delta s}$	$= \frac{C_0^\tau - C_1^\tau}{8} - \frac{C_0^{\Delta\rho} + C_1^{\Delta\rho}}{6},$
$C_0^J$	$= \frac{1}{12}(C_0^\tau - 3C_1^\tau - 16C_1^{\Delta\rho}),$
$C_1^J$	$= -\frac{1}{12}(C_0^\tau - 3C_1^\tau),$
$C_1^{\nabla J}$	$= C_0^{\nabla J}.$

Table 3: Restrictions on the parameters of the general SHF functional (6) in case that the functional is derived from the Skyrme force ansatz (36).

ical analysis see [26, 27, 28, 29]. The development of the spin branch in SHF is still in its first stages, this means in the language of section 5 at the preparatory level of point 1, although one can find also some steps of the error analysis according to point 3 and sub-points 3.1 together with 3.4 therein. This latter aspect will shine up briefly in the subsequent example of odd nuclei and of TDHF. But generally, the aim of the present section is mainly to demonstrate the capabilities of SHF to deal also with spin properties.

Before going on, we have to look at the spin aspects of the basic SHF functional (6), so far not discussed. Some spin terms, namely the time odd spin-orbit terms  $\propto C_T^{\nabla J}$  in the time-odd part of the functional (6c), are fixed by the requirement of Galilean invariance. Yet open remain the parameters of the genuine spin terms  $C_T^\sigma$  and the tensor spin-orbit terms  $\propto C_T^J$ . From a strictly density functional perspective, one can consider these all as free parameters of the model. This leaves still a large number of 7 more free parameters whose independent calibration would require access to a great amount of reliable, spin-sensitive data. Alternatively, one can approach the problem from a formal side. The density-matrix expansion sketched in section 2.3 yields not directly an energy functional, but rather a zero-range effective interaction, the much celebrated Skyrme force. For its detailed form and a critical discussion of the notion of an effective interaction see appendix A. Deriving the SHF functional from the Skyrme force yields a well defined connection between the spin terms and the leading terms, see table 3. These restrictions on the spin-orbit parameters from the force definition of the SHF functional are often discarded. Many parametrizations simply ignore the tensor spin-orbit terms, thus supposing  $C_0^J = 0$  and  $C_1^J = 0$ . There are also reasons to override the restriction on the spin-orbit parameter  $C_1^{\nabla J} = C_0^{\nabla J}$  [104]. All functionals used in this paper ignore the tensor spin-orbit terms and treat  $C_1^{\nabla J}$  as independent parameter. The spin gradient terms  $\propto C_T^{\Delta s}$  when taken as given in table 3 lead for most functionals to dramatic instabilities. They must be discarded. What remains then from the force concept is the parameter connection from Galilean invariance and the determination of the pure spin terms  $\propto C_T^\sigma$ . Galilean invariance is the unavoidable minimum requirement and



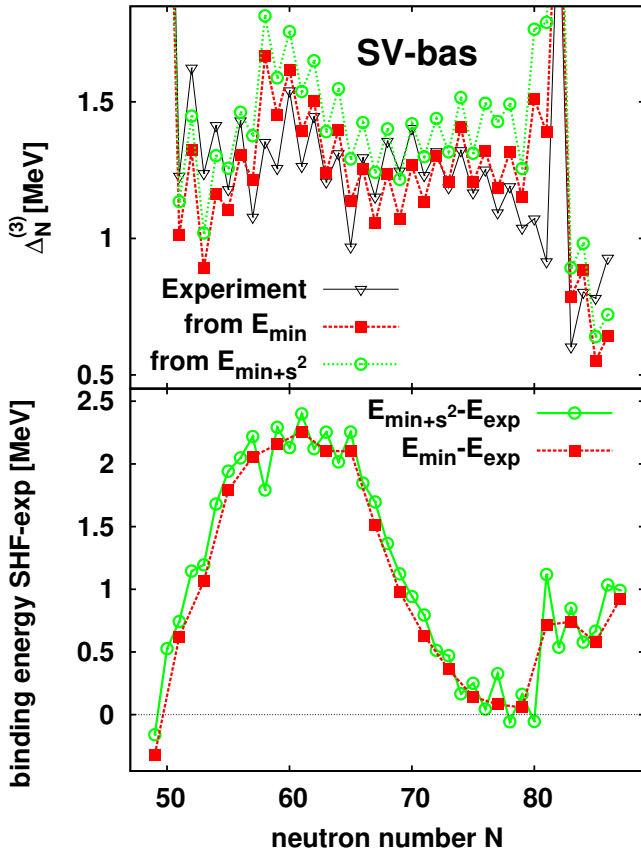


Fig. 15: Difference of theoretical and experimental binding energies (lower panel) and neutron odd-even staggering  $\Delta_N^{(3)}$  (upper panel) along the isotopic chain of Sn nuclei computed with the parametrization SV-bas [32]. The  $E_{\min}$  stands for the minimal Galileo invariant functional and  $E_{\min,\sigma^2}$  for the functional including additionally the  $\sigma^2$  terms according to the force definition, see table 3. Data extracted from [113].

will always be used. Above that we have the freedom to employ the spin and/or tensor spin-orbit terms. Although one cannot take the full “force” terms consistently into account, it is convenient to exploit it for the spin terms and the tensor spin-orbit part yielding the connections as given in table 3. As this is an ad-hoc decision, justification can come only from experience.

As a first example, we address odd nuclei picking a key result from [113]. Figure 15 shows the deviation of binding energies from experimental values and the odd-even staggering (19) along the chain of Sn isotopes. Two stages of the functional are considered, the minimal Galilean invariant form  $E_{\min}$  corresponding to  $C_T^\sigma = 0$  and the inclusion is the  $\sigma_T^2$  terms with parameters as given in table 3. The trend of the binding (lower panel) is generally very similar for odd and even isotopes. There is a good reproduction in the region  $N = 70 - 82$ . The larger deviations mid shell indicate that these nuclei require collective correlations (not included here) for a proper description. Odd nuclei make no difference in that respect. Of course, both variants yield the same values for even isotopes because the time-odd terms are inactive there. It remains to look at differences for odd isotopes. The effect of the spin terms is small, of the order of 0.2 MeV and in the majority of cases enhancing slightly the deviations. Thus the results for binding energies give a slight preference for the  $E_{\min}$

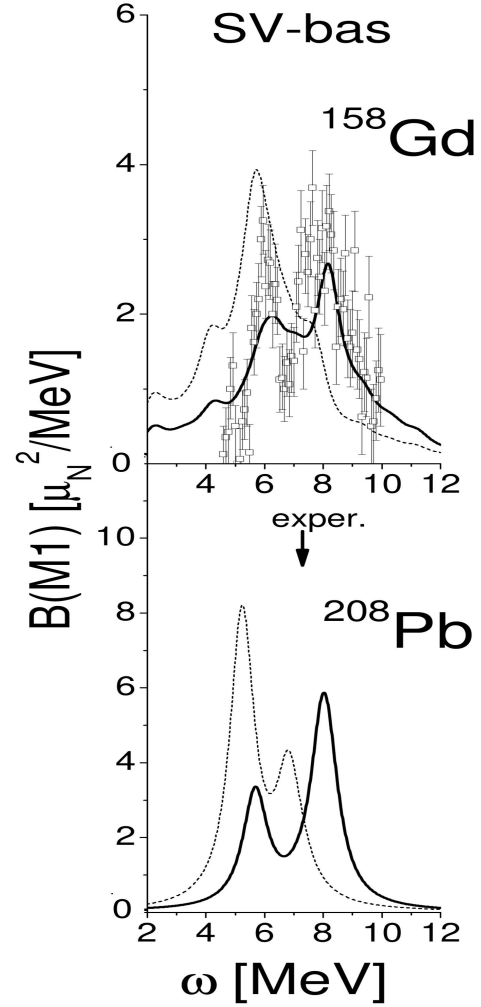


Fig. 16: Isoscalar M1 strength distribution for the spin-flip mode in deformed  $^{158}\text{Gd}$  and the spherical  $^{208}\text{Pb}$  computed with separable RPA using the parametrization SV-bas. The RPA results are shown by heavy line and the strength distribution from pure two-quasiparticle excitations (from static mean field only) by faint lines. The experimental distribution is shown for  $^{158}\text{Gd}$ . The remarked experimental resonance peak is indicated by an arrow for  $^{208}\text{Pb}$ . Adapted from [120].

model.

The upper panel of figure 15 shows the odd-even staggering. It is very satisfying that the parametrization SV-bas provides at once a satisfying reproduction of the data. At a more detailed level, we see differences between the two choices for the spin terms. There are cases where  $E_{\min,\sigma^2}$  performs better (particularly at the side of small  $N$ ). But, again, we find that the majority of isotopes looks better with the minimal Galilean invariant choice  $E_{\min}$ . This slight preference for  $E_{\min}$  was also found for other examples and other parametrizations [113]. But the differences are probably too small to be decisive and more studies are still necessary to settle the case. Recall that the most important result of this brief demonstration is that the SHF functional yields immediately an acceptable description also of odd nuclei.

Figure 16 shows as next example a result for spin excitations, here the M1 strength distribution of the spin-flip mode, computed including the spin terms of the SHF functionals. Two rather different nuclei are considered, the

well deformed mid-shell nucleus  $^{158}\text{Gd}$  and the spherical, doubly magic  $^{208}\text{Pb}$ . The RPA result is shown together with the mere two-quasiparticle excitations (i.e. without the dynamical effects from the RPA residual interaction [109]). One sees a marked upshift of strength by RPA (also called collective shift) due to the repulsive residual interaction in the isoscalar spin channel. This upshift brings indeed the strengths into the right energy range. Thus far we see once more that a proper SHF functional is also appropriate for spin modes, at least what gross features is concerned. Looking closer at the case, we see a problem. The experimental distribution differs between deformed and spherical nuclei. It has two pronounced peaks for the deformed  $^{158}\text{Gd}$  but only one for the spherical  $^{208}\text{Pb}$ . The theoretical result shows a two-peak structure for both cases. This has been studied extensively in [116, 120] for a broad selection of SHF parametrizations. There are some parametrizations which produce one single peak for  $^{208}\text{Pb}$ , but then one peak only also for  $^{158}\text{Gd}$ . With presently available functionals it seems impossible to describe both nuclei equally well. The source of the problem lies most probably in an incomplete inclusion of spin-orbit terms. A satisfying solution has yet to be worked out.

Finally we demonstrate the enormous capabilities of self-consistent mean field theories by examples from time-dependent Hartree-Fock (TDHF). TDHF allows to simulate a wide range of nuclear processes covering resonance dynamics, non-linear excitations, and particularly large amplitude motion with substantial rearrangement of structure in the course of time as it occurs, e.g., in heavy-ion reactions. First nuclear TDHF calculations came up already shortly after the appearance of static SHF calculations [121]. Two decades ago, TDHF has been revived because computing capabilities had evolved sufficiently far to allow realistic large-scale calculations, for examples of a couple of very different applications see [122, 123, 124, 125]. A combination of TDHF with density-constrained Hartree-Fock even allows to compute sub-barrier fusion cross sections [126, 127]. Stepping forward to still larger scales, TDHF is now being applied to simulate matter under astro-physical conditions in neutron stars and super-nova explosions [128, 129]. For recent reviews on TDHF with SHF functionals see [130, 131]. In all these applications, one found that SHF functionals provide at once a fair description of the processes studied. There are open ends though because spin terms can play a role in energetic collisions and we have seen above that just these terms are not yet well settled. We will exemplify in the following both, the capabilities and the uncertainties of TDHF simulations.

Figure 17 shows snapshots of the Wigner function from a TDHF simulation of a central collision  $^{16}\text{O}+^{16}\text{O}$  [132]. The simulation was performed on a Cartesian 3D mesh, for details of the physics and numerics of TDHF and the 3D code see [131]. The Wigner function is constructed from the one-body density matrix  $\varrho(\mathbf{r}, \mathbf{r}')$  by Fourier transforming with respect to  $\mathbf{y} = \mathbf{r} - \mathbf{r}'$ , i.e.  $f(\bar{\mathbf{r}}, \mathbf{k}) = \int d^3y e^{i\mathbf{k}\cdot\mathbf{y}} \varrho(\bar{\mathbf{r}} + \mathbf{y}/2, \bar{\mathbf{r}} - \mathbf{y}/2)$ . Originally introduced in [133], it is the attempt to provide a phase-space picture of a quantum state, for details see [134]. The Wigner function has the weakness that it is not positive semi-definite, thus preventing a strict probabilistic inter-

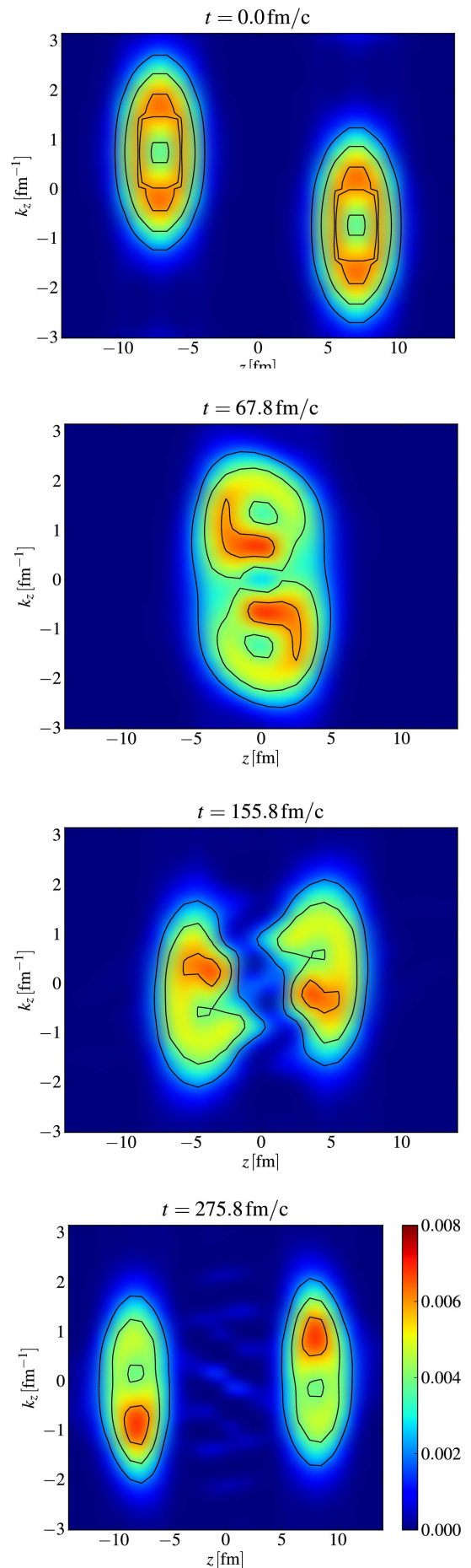


Fig. 17: Snapshots of the Wigner distribution in the  $z$ - $k_z$ -plane from a TDHF simulation of a central  $^{16}\text{O}+^{16}\text{O}$  collision using the parametrization SkI3 [104]. Adapted from [132].



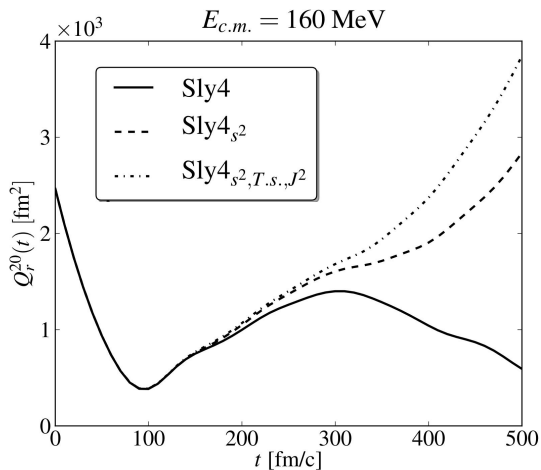


Fig. 18: Time evolution of the quadrupole momentum  $Q_{20}$  for a central collision  $^{40}\text{Ca}+^{40}\text{Ca}$  computed for the parametrization SLy4 [137] with three different options for the spin terms as indicated. Adapted from [138].

pretation. Nonetheless, it can serve as a useful illustration of a dynamical process and the availability of all detailed wavefunctions in a TDHF calculation allows us to produce this insight. The Wigner function in a 3D calculation is six-dimensional and thus rather difficult to handle. We thus look at a 2D cut through the 6D function, namely along the reaction axis  $z$  and associated wavenumber  $k_z$ . The snapshots are sorted from above to below in order of increasing time. The initial stage shows nicely the two Fermi spheres of the  $^{16}\text{O}$  nuclei, unperturbed except for the c.m. boost to positive  $k_z$  for the left nucleus and to negative  $k_z$  for the right one. The second panel shows the situation at the point of closest contact. Although the corresponding local density represents a compact compound system, the phase space picture shows that the compound stage has not lost its memory at the initial state. There are two distinct fragments in phase space. This feature persists to the next plot the fragments separating. They are strongly perturbed, but kept their identity from the initial nuclei. And in the final stage (lowest panel), two fragments are flying apart, internally excited and with reduced c.m. motion, but still keeping the two-fragment structure of the initial state. This indicates that pure mean-field motion does not allow full melting into one thermal compound state. This becomes possible only if two-body collisions are added to the description. This is achieved in the semi-classical framework by the Vlasov-Uehling-Uhlenbeck scheme [135]. Adding a collision term to quantum mechanical TDHF turns out to be much more involved, although just recently promising attempts have come up [136]. This example indicates that TDHF dynamics is likely to underestimate dissipation processes. It still provides relevant guidelines for the gross structure of a process and can be even quantitatively correct in the entrance state of a heavy-ion reaction where nucleon-nucleon collisions did not yet have a chance to play a role. For example, one can describe very well fusion cross sections with TDHF, see e.g. [126].

Figure 18 shows the result from a TDHF calculation for a central collision of  $^{40}\text{Ca}+^{40}\text{Ca}$  at relative center of mass

energy 240 MeV [138]. Shown is the quadrupole momentum along the reaction axis as function of time. This quantifies the relative distance of the fragments and illustrates the type of reaction as well as damping of c.m. motion. In this case, three different choices for the SHF functional are compared: The parametrization SLy4 just with the minimal Galilean invariant terms, SLy4 with the  $\sigma^2$  terms included, and SLy4 with  $\sigma^2$  plus tensor spin-orbit terms included. Unlike the case of ground states of odd nuclei, we see in this highly dynamical case a great sensitivity to the spin and spin-orbit terms. Their inclusion turns a fusion dynamics (heavy line for SLy4 without spin terms) to inelastic scattering which means that they reduce dissipation. It ought to be mentioned, however, that the leading spin orbit term  $\propto C_T^{\nabla J}$  acts in different direction, significantly enhancing dissipation [139, 140]. Thus there is a very subtle interplay of the various terms in the SHF functional. With the new generation of computers and codes, one will now be in a position to systematically investigate the intrinsic structure of heavy-ion reactions. And, as in all previous example of this section, we emphasize that the SHF functional delivers in general a relevant picture of structure and dynamics also for cases where spin plays a role. This is a safe basis for then going into details.

## 7. Concluding remarks

The Skyrme-Hartree-Fock (SHF) model for a self-consistent mean-field description of nuclear structure and dynamics has been inspected from different perspectives: formal background, range of applicability, performance, estimates of extrapolation uncertainties, and correlation (covariance) between different observables. SHF is based on an effective energy-density functional which is formally motivated by a low-momentum expansion of a most general effective interaction and its free parameters are calibrated by a fit to empirical data, mostly from nuclear ground states. This mixed origin calls for particularly careful exploration of the capability, reliability, and limits of the model. One key task is to estimate the uncertainties in extrapolations. Related to that is the other task to find out the dependencies between observables (and model parameters) which helps to identify, e.g., bottlenecks in the model and to cure them. A great manifold of strategies to attack these task was outlined in section 5. A large part of them was exemplified in the subsequent result section. The same pool of fit data was used in all examples to render the tests consistent with each other and so maintain comparability. These data were bulk properties of nuclear ground states in chains of semi-magic nuclei selected to be good mean-field nuclei (only very small effects from collective ground-state correlations). We summarize the basic findings of that survey in key sentences:

1. There is no single ideal strategy to estimate the uncertainties in predictions from a model. A bundle of different methods has to be invoked to develop a sound intuition for the limits and capabilities of a model. Statistical analysis in connection with  $\chi^2$  fits is one important part. Harder is an estimate of the systematic error. It has to be approached from different sides, formal analysis as well as variations of the model, and yet will always leave open ends.

2. Concerning the basic performance, modern SHF functionals have reached a high quality of description of ground state properties in the whole known nuclear landscape, from light nuclei, as  $^{16}\text{O}$ , up to super-heavy elements. For example, energies are reproduced with a r.m.s error of about 0.6 MeV.
3. Although not explicitly fitted for that, modern SHF functionals can be used successfully for many other observables and processes as resonance excitations, astro-physical nuclear matter, nuclear rotation at high spin, and large-amplitude collective motion (low-energy quadrupole vibrations, fission, fusion, heavy-ion scattering). The latter example goes, in fact, often beyond a mere mean-field treatment.
4. Although small, the residual errors are not statistically distributed, but show still unresolved trends as typical fluctuations between doubly-magic and mid-shell nuclei and, more puzzling, a small but systematic increase of under-binding towards heavy and super-heavy nuclei. The latter trend is probably due to yet insufficient modeling of density dependence of the SHF functional.
5. Extrapolation errors from statistical analysis provide a lower estimate (yet without contributions from systematic errors) which is already extremely useful to distinguish safe and risky extrapolations. Not surprisingly, errors increase with increasing distance to the fit data. For example, extrapolations to super-heavy elements are still found to be reliable while error bars grow huge when predicting properties of neutron stars. On the other hand, interpolations in the vicinity of the fit data are safe and yield deviations as small as the average errors in the fit pool.
6. There is a hierarchy of importance within the terms of the SHF functional. From a formal side, importance shrinks with increasing order of derivatives involved. From the empirical side, isoscalar properties are better determined than isovector ones due to the limited extension of known nuclei along isotopic chains. Taking the most important terms delivers a minimal model with only 6 free parameters which provides already the high quality of ground state properties as the final model employing all 11 free parameters of the SHF functional. The further terms above the minimal model serve to optimize further features as, e.g., giant resonance excitations.
7. The impact of the fit data was checked by performing fits with successively omitting a group of data. From the four groups of fit data (binding energy  $E_B$ , charge r.m.s. radius  $r_{\text{rms}}$ , charge diffraction radius  $R_{\text{diff}}$ , charge surface thickness  $\sigma_C$ ),  $E_B$  is found to be the most decisive one. Fits with  $E_B$  alone yield already an acceptable model. Adding  $r_{\text{rms}}$  to the pool of  $E_B$  comes another step closer to the full fit while considering  $r_{\text{rms}}$  alone is insufficient. The small drifts of average errors and of predicted observables when adding  $R_{\text{diff}}$  and  $\sigma_C$  shows that each group pulls the fit into a slightly different direction. This conflict between observables points to a rigidity in modeling the nuclear surface profile which, again, is probably related to the modeling of density dependence.
8. A particularly instructive analyzing tool is the systematic variation of model features, here exemplified by the variation of nuclear matter parameters (NMP). It illustrates the impact of such a parameter on an observable of interest. This allowed to demonstrate the near one-to-one correspondence of NMP and giant resonances in  $^{208}\text{Pb}$ , namely incompressibility  $K$  with the giant monopole resonance, isoscalar effective mass  $m^*/m$  with the giant quadrupole resonance, symmetry energy  $J$  with the dipole polarizability  $\alpha_D$ , and the TRK sum-rule enhancement  $\kappa_{\text{TRK}}$  (alias isovector effective mass) with the giant dipole resonance. A much different behaviour is seen for fission barrier and lifetime in the super-heavy nucleus  $^{266}\text{Hs}$ . These observables gather influences from many different parameters and have no prevailing correlation.
9. Ab-initio data are not yet regularly included in the calibration of the SHF functional. As an example for ab-initio input, the neutron gas at very low density was considered. This data point can meanwhile be computed very well with the theory of the correlated Fermi gas (CFG) and it is exclusively determined by long range correlations from zero-sound modes of the gas. It turns out that the standard SHF functional is not able to accommodate this data point from CFG. A new density dependent term must be added to allow an adjustment which then works acceptably well. The extended model allows also to test the effect of an additional density dependence when fitting to the standard pool of data (excluding the CFG point). This fit resolves the conflict between observables discussed under point 7 thus confirming that modeling of density dependence is still an issue.
10. Correlation (or covariance) analysis was exemplified for a small selection of relevant observables covering the four essential groups of response properties, isoscalar static, isoscalar dynamic, isovector static, and isovector dynamic. This confirmed very clearly the one-to-one correspondence between NMP and giant resonance, already worked out under point 8. Noteworthy is a large block of isovector static observables covering, beside  $J$  and  $\alpha_D$ , the neutron skin, pure neutron matter, and the slope of symmetry energy  $L$ . All these relations are rather robust under changing conditions of modeling and selection of fit data.
11. Spin terms in the SHF functional leave still open questions. A part of them is determined by the requirement of Galilean invariance. Other terms can be fixed by the concept of a Skyrme “force”. But this setting often leads to principle instabilities in the spin channel. Particularly dangerous are the spin-gradient terms which thus are discarded in all applications. There remains, again, a decision based on empirical data. The case is not yet settled and requires further research.

12. The pairing part of the functional has not been discussed in this paper. Similar as the spin terms, it is also not yet fully explored. The present form is optimized to reproduce the odd-even staggering in isotopic and isotonic chains of semi-magic nuclei and serves to produce well defined ground states for open shell nuclei. Pairing is found to have a large impact on low-lying quadrupole excitations and fission. This may require still a further fine tuning for such processes.

13. As mentioned in point 3, the SHF functional is often successful even in applications beyond pure mean field. Such methods require the energy overlap between different mean field states. These can be evaluated with the SHF functional as long as the different states remain close (Gaussian overlap approximation). However, projection onto good particle number or angular momentum require also overlaps between remote states and the SHF functional in its standard form become inapplicable for this task. New modeling based strictly on a force concept is needed, and underway to resolve this problem.

Altogether, the SHF functional has proven to deliver an extremely useful and reliable reproduction of static and dynamic features of nuclei as far as they are accessible to a mean-field description. One could be highly satisfied with what has been achieved. However, the success shows the capability of SHF and motivates to ask for more. Such more is also highly desirable in view of the the remarkable progress in producing exotic nuclei and of the far extrapolations implied in astro-physical applications (extremely neutron rich isotopes in the  $r$ -process, neutron stars, nuclear matter under supernova conditions). Work on further scrutinizing and improving the SHF functional along the lines summarized above is in progress in many research groups around the world.

**Acknowledgment:** This work has been supported by a grant from the German ministry of Science and Technology, grant number 05P12RFFTG, and from the Deutsche Forschungsgemeinschaft, grant number RE 322-14/1.

## A. The Skyrme force

The SHF functional was motivated in section 2.3 through the density-matrix expansion [49, 50, 31]. This expansion acts on a supposed microscopic interaction, the  $T$  matrix from some ab-initio model, and delivers the “Skyrme

force” in the form (tensor terms are ignored here)

$$\begin{aligned}\hat{V}_{\text{Sk}} = & t_0(1+x_0\hat{P}_\sigma)\delta(\mathbf{r}_{12}) \\ & + \frac{t_3}{6}(1+x_3\hat{P}_\sigma)\rho^\alpha(\mathbf{r}_1)\delta(\mathbf{r}_{12}) \\ & + \frac{t_1}{2}(1+x_1\hat{P}_\sigma)\left(\delta(\mathbf{r}_{12})\hat{\mathbf{k}}^2 + \hat{\mathbf{k}}'^2\delta(\mathbf{r}_{12})\right) \\ & + t_2(1+x_2\hat{P}_\sigma)\hat{\mathbf{k}}'\delta(\mathbf{r}_{12})\hat{\mathbf{k}} \\ & + it_4(\hat{\boldsymbol{\sigma}}_1 + \hat{\boldsymbol{\sigma}}_2) \cdot \hat{\mathbf{k}}' \times \delta(\mathbf{r}_{12})\mathbf{k} \quad ,\end{aligned}\quad (36)$$

$$\mathbf{r}_{12} = \mathbf{r}_1 - \mathbf{r}_2 \quad ,$$

$$\hat{P}_\sigma = \frac{1}{2}(1 + \hat{\boldsymbol{\sigma}}_1\hat{\boldsymbol{\sigma}}_2) \quad ,$$

$$\hat{\mathbf{k}} = -\frac{i}{2}\left(\vec{\nabla}_1 - \vec{\nabla}_2\right) \quad , \quad \hat{\mathbf{k}}' = \frac{i}{2}\left(\overleftarrow{\nabla}_1 - \overleftarrow{\nabla}_2\right) \quad .$$

where  $\hat{\mathbf{k}}$  acts to the right and  $\hat{\mathbf{k}}'$  to the left. We put the notion “force” in quotation mark because this object depends on the density which is produced by the wave function on which this force acts. This is not a standard two-body interaction, but an effective force designed for the only purpose to derive an energy functional (for a detailed discussion of the principle problems see [69]). The evaluation of the expectation value of  $\hat{V}_{\text{Sk}}$  with a BCS state yields indeed a functional of the form (6). In fact, it yields more than that. The 10 parameters of the “force” (36) are distributed over the 23 parameters of the SHF functional (when counting each term with a separate free parameter). This establishes a couple of relations between the parameters of the SHF functional. They embrace, of course, the restriction from Galilean invariance already embodied in the time-odd part (6c) and add seven more relations which fix all spin terms as shown in table 3.

It is interesting to note that the Skyrme force is particularly restrictive with respect to the spin-orbit terms. The tensor spin-orbit terms  $\propto \mathbb{J}^2$  are fully determined by the kinetic terms as  $C_T^J$  is given by  $C_T^T$  and  $C_T^{\Delta\rho}$  and the  $C_1^{\nabla J} = C_0^{\nabla J}$  ties the isovector to the isoscalar spin-orbit term. The first restriction is neither harmful nor beneficial as this tensor spin-orbit term can easily be compensated by the normal spin-orbit term. The second restriction is more serious and to some extent questioned by phenomenology [104]. Most traditional parametrizations employ this restriction. Recent fits, particularly those following [32] discard the restriction to maintain independence of the isovector spin-orbit parameter.

## B. Pool of fit data

Table 4 summarizes the pool of data as defined in [32]. These data were used to determine SV-min, SV-bas and the series of forces with systematically varied NMP (used here, e.g., in section 6.3). They are used for the new fits in this paper, see e.g. sections 6.2 or 6.4. The detailed values for the listed observables are found in the original paper [32].

## References

## References

- [1] A. Bohr, Rev. Mod. Phys. 48 (1975) 365.

$E$ :	$^{36-52}\text{Ca}, ^{68}\text{Ni}, ^{100,126-134}\text{Sn}, ^{204-214}\text{Pb},$ $^{34}\text{Si}, ^{36}\text{S}, ^{38}\text{Ar}, ^{50}\text{Ti}, ^{86}\text{Kr}, ^{88}\text{Sr}, ^{90}\text{Zr},$ $^{92}\text{Mo}, ^{94}\text{Ru}, ^{96}\text{Pd}, ^{98}\text{Cd}, ^{134}\text{Te}, ^{136}\text{Xe},$ $^{138}\text{Ba}, ^{140}\text{Ce}, ^{142}\text{Nd}, ^{144}\text{Sm}, ^{146}\text{Gd},$ $^{148}\text{Dy}, ^{150}\text{Er}, ^{152}\text{Yb}, ^{206}\text{Hg}, ^{210}\text{Po},$ $^{212}\text{Rn}, ^{214}\text{Ra}, ^{216}\text{Th}, ^{218}\text{U}$
$R_{\text{diff}}$ :	$^{16}\text{O}, ^{40-44,48}\text{Ca}, ^{58-64}\text{Ni}, ^{118-124}\text{Sn},$ $^{204-208}\text{Pb}, ^{50}\text{Ti}, ^{52}\text{Cr}, ^{54}\text{Fe}, ^{86}\text{Kr},$ $^{88}\text{Sr}, ^{90}\text{Zr}, ^{92}\text{Mo}, ^{138}\text{Ba}, ^{142}\text{Nd},$
$\sigma$ :	$^{16}\text{O}, ^{40-44,48}\text{Ca}, ^{60-64}\text{Ni}, ^{118,122-124}\text{Sn},$ $^{204-208}\text{Pb}, ^{50}\text{Ti}, ^{86}\text{Kr}, ^{88}\text{Sr}, ^{90}\text{Zr},$ $^{92}\text{Mo}, ^{138}\text{Ba}, ^{142}\text{Nd},$
$r_{\text{rms}}$ :	$^{16}\text{O}, ^{40-48}\text{Ca}, ^{108,118-124}\text{Sn}, ^{200-214}\text{Pb},$ $^{36}\text{S}, ^{38}\text{Ar}, ^{50}\text{Ti}, ^{52}\text{Cr}, ^{54}\text{Fe}, ^{86}\text{Kr}, ^{88}\text{Sr},$ $^{90}\text{Zr}, ^{92}\text{Mo}, ^{136}\text{Xe}, ^{138}\text{Ba}, ^{140}\text{Ce},$ $^{142}\text{Nd}, ^{144}\text{Sm}, ^{146}\text{Gd}, ^{148}\text{Dy}, ^{150}\text{Er},$ $^{206}\text{Hg}, ^{210}\text{Po}, ^{212}\text{Rn}, ^{214}\text{Ra},$
$\Delta^{(3)}$	isotopes $Z=50,82$ and isotones $N=50,82$
$l^*s$ :	$^{16}\text{O}(1p_n, 1p_p) \ ^{132}\text{Sn}(2p_p, 2d_n),$ $^{208}\text{Pb}(2d_p, 1f_n, 3p_n)$
$\delta r^2$ :	isotope shift $r^2(^{214}\text{Pb}) - r^2(^{208}\text{Pb})$
NMP:	$K, m^*/m, \kappa_{\text{TRK}}, a_{\text{sym}}$ (only SV-bas)

Table 4: Compilation of phenomenological input from [32] used for the fits of the various parametrizations presented in this paper. Abbreviations mean:  $E$  = binding energy,  $r$  = charge r.m.s. radius,  $R$  = charge diffraction radius,  $\sigma$  = charge surface thickness,  $l^*s$  = spin-orbit splitting of selected single-particle states,  $\delta r^2$  = isotopic shift of charge radii, and NMP = nuclear matter properties (in symmetric matter).

[2] B. Mottelson, Rev. Mod. Phys. 48 (1975) 375.  
[3] J. Rainwater, Rev. Mod. Phys. 48 (1975) 385.  
[4] Å. Bohr, B. R. Mottelson, Nuclear Structure: Vols. I & II, World Scientific, Singapur, 1999.  
[5] P. Möller, J. R. Nix, W. D. Myers, W. J. Swiatecki 59 (1995) 185.  
[6] T. H. R. Skyrme, Nucl. Phys. 9 (1959) 615.  
[7] D. Vautherin, D. M. Brink, Phys. Rev. C 5 (1972) 626.  
[8] D. Gogny, P. Pires, R. De, Tourreil, Phys. Lett. B 32 (1970) 591.  
[9] J. Dechargé, D. Gogny, Phys. Rev. C 21 (1980) 1568.  
[10] B. D. Serot, J. D. Walecka, Ann. Rev. Nuc. Phys. 16 (1986) 1.  
[11] P.-G. Reinhard, Rep. Prog. Phys. 52 (1989) 439.  
[12] D. Vretenar, A. Afanasjev, G. Lalazissis, P. Ring, Phys. Rep. 409 (2005) 101.  
[13] M. Bender, P.-H. Heenen, P.-G. Reinhard, Rev. Mod. Phys. 75 (2003) 121.  
[14] P. Hohenberg, W. Kohn, Phys. Rev. 136 (1964) 864.

[15] W. Kohn, L. J. Sham, Phys. Rev. 140 (1965) 1133.  
[16] J. P. Perdew, K. Burke, M. Ernzerhof, Phys. Rev. Lett. 77 (1996) 3865.  
[17] W. H. Dickhoff, H. Müther, Rep. Prog. Phys. 55 (1992) 1947.  
[18] V. R. Pandharipande, I. Sick, P. K. A. deWitt Huberts, Rev. Mod. Phys. 69 (1997) 981.  
[19] E. Epelbaum, H.-W. Hammer, U.-G. Meiner, Rev. Mod. Phys. 81 (2009) 1773.  
[20] R. Machleidt, D. R. Entem, Phys. Rep. 503 (2011) 1.  
[21] H.-W. Hammer, A. Nogga, A. Schwenk, Rev. Mod. Phys. 85 (2013) 197.  
[22] R. M. Dreizler, E. K. U. Gross, Density Functional Theory: An Approach to the Quantum Many-Body Problem, Springer-Verlag, Berlin, 1990.  
[23] J. Messud, M. Bender, E. Suraud, Phys. Rev. C 80 (2009) 054314.  
[24] Y. M. Engel, D. M. Brink, K. Goeke, S. J. Krieger, D. Vautherin, Nucl. Phys. A 249 (1975) 215.  
[25] P. Ring, Prog. Part. Nuc. Phys. 37 (1996) 193.  
[26] T. Lesinski, M. Bender, K. Bennaceur, T. Duguet, J. Meyer, Phys. Rev. C 76 (2007) 014312.  
[27] M. Bender, K. Bennaceur, T. Duguet, P.-H. Heenen, T. Lesinski, J. Meyer, Phys. Rev. C 80 (2009) 064302.  
[28] D. Davesne, M. Martini, K. Bennaceur, J. Meyer, Phys. Rev. C 80 (2009) 024314.  
[29] V. Hellemans, A. Pastore, T. Duguet, K. Bennaceur, D. Davesne, J. Meyer, M. Bender, P.-H. Heenen, Phys. Rev. C 88 (2013) 064323.  
[30] P.-G. Reinhard, E. W. Otten, Nucl. Phys. A420 (1984) 173.  
[31] P.-G. Reinhard, C. Toepffer, Int. J. Mod. Phys. E 3 (1994) 435.  
[32] P. Klüpfel, P.-G. Reinhard, T. J. Bürvenich, J. A. Maruhn, Phys. Rev. C 79 (3) (2009) 034310.  
[33] P. Ring, P. Schuck, The Nuclear Many-Body Problem, Springer-Verl., New York, Heidelberg, Berlin, 1980.  
[34] J. Dobaczewski, H. Flocard, J. Treiner, Nucl. Phys. A 422 (1984) 103.  
[35] P. Bonche, H. Flocard, P.-H. Heenen, S. J. Krieger, M. S. Weiss, Nucl. Phys. A 443 (1985) 39.  
[36] S. J. Krieger, P. Bonche, H. Flocard, P. Quentin, M. S. Weiss, Nucl. Phys. A 517 (1990) 275.  
[37] M. Bender, K. Rutz, P.-G. Reinhard, J. A. Maruhn, Eur. Phys. J. A 8 (2000) 59.

- [38] M. Bender, K. Rutz, P.-G. Reinhard, J. Maruhn, Eur. Phys. J A 7 (2000) 467.
- [39] J. Erler, P. Klüpfel, P.-G. Reinhard, J. Phys. G 38 (2011) 033101.
- [40] K. Schmid, P.-G. Reinhard, Nucl. Phys. A 530 (1991) 283.
- [41] P. Klüpfel, J. Erler, P.-G. Reinhard, J. A. Maruhn, Eur. Phys. J. A 37 (2008) 343.
- [42] P.-G. Reinhard, Z. Phys. A 285 (1978) 93.
- [43] K. Hagino, P.-G. Reinhard, G. Bertsch, Phys. Rev. C 65 (2002) 064320.
- [44] M. Bender, G. F. Bertsch, P.-H. Heenen, Phys. Rev. Lett. 94 (2005) 102503.
- [45] M. Bender, G. F. Bertsch, P.-H. Heenen, Phys. Rev. C 73 (2006) 034322.
- [46] P.-G. Reinhard, K. Goeke, Rep. Prog. Phys. 50 (1987) 1.
- [47] J. Dobaczewski, M. Stoitsov, W. Nazarewicz, P.-G. Reinhard, Phys. Rev. C 76 (2007) 054315.
- [48] F. Raimondi, K. Bennaceur, J. Dobaczewski, J. Phys. G 41 (2014) 055112.
- [49] J. W. Negele, D. Vautherin, Phys. Rev. C 5 (1972) 1472.
- [50] J. W. Negele, D. Vautherin, Phys. Rev. C 11 (1975) 1031.
- [51] A. Duncan, The conceptual framework of quantum field theory, Oxford University Press, Oxford, 2012.
- [52] W. D. Myers, Droplet Model of Atomic Nuclei, IFI/Plenum, New York, 1977.
- [53] R. W. Hasse, W. D. Myers, Geometrical Relationships of Macroscopic Nuclear Physics, Springer, Berlin, Heidelberg, New York, 1988.
- [54] P.-G. Reinhard, M. Bender, W. Nazarewicz, T. Vertse, Phys. Rev. C 73 (2006) 014309.
- [55] D. J. Thouless, The Quantum Mechanics of Many-Body Systems, Academic Press, New York, 1961.
- [56] W. Nazarewicz, P.-G. Reinhard, W. Satula, D. Vretenar, Eur. Phys. J. A 50 (2014) 20.
- [57] J. Friedrich, N. Vöglér, Nucl. Phys. A 373 (1982) 192.
- [58] J. L. Friar, J. W. Negele, Adv. Nuc. Phys. 8 (1975) 219.
- [59] G. G. Simon, C. Schmitt, F. Borkowski, V. H. Walther, Nucl. Phys. A 333 (1980) 381.
- [60] V. H. Walther, private communication (1986).
- [61] P.-G. Reinhard, Phys. Lett. A 169 (1992) 281.
- [62] C. J. Batty, E. Friedman, H. J. Gils, H. Rebel, Adv. Nuc. Phys. 19 (1989) 1.
- [63] C. J. Horowitz, S. J. Pollock, P. A. Souder, R. Michaels, Phys. Rev. C 63 (2001) 025501.
- [64] B. C. Clark, L. J. Kerr, Phys. Rev. E 68 (2003) 031204.
- [65] P.-G. Reinhard, W. Nazarewicz, Phys. Rev. C 81 (5) (2010) 051303.
- [66] P.-G. Reinhard, Y. Gambhir, Ann. Phys. (Leipzig) 504 (1992) 598.
- [67] P.-G. Reinhard, Ann. Phys. (Leipzig) 504 (1992) 632.
- [68] N. Lyutorovich, V. Tselyaev, J. Speth, S. Krewald, F. Grümmer, P.-G. Reinhard, Phys. Lett. B to appear.
- [69] J. Erler, P. Klüpfel, P.-G. Reinhard, J. Phys. G 37 (2010) 064001.
- [70] N. Lyutorovich, V. Tselyaev, J. Speth, S. Krewald, F. Grümmer, P.-G. Reinhard, Phys. Rev. Lett. 109 (2012) 092502.
- [71] A. Tamii, *et al.*, Phys. Rev. Lett. 107 (2011) 062502.
- [72] T. Hashimoto, *et al.*, Phys. Rev. C to appear.
- [73] N. Schindzielorz, J. Erler, P. Klüpfel, P.-G. Reinhard, G. Hager, Int. J. Mod. Phys. E 18 (2009) 773.
- [74] J. Erler, K. Langanke, H. P. Loens, G. Martinez-Pinedo, P.-G. Reinhard, Phys. Rev. C 85 (2012) 025802.
- [75] A. Baran, M. Kowal, P.-G. Reinhard, L. Robledo, A. Staszczak, M. Warda, Nucl. Phys. A to appear.
- [76] P. R. Bevington, D. K. Robinson, Data Reduction and Error Analysis for the Physical Sciences, McGraw-Hill, 2003.
- [77] J. Friedrich, P.-G. Reinhard, Phys. Rev. C 33 (1986) 335.
- [78] T. Niksic, D. Vretenar, G. Lalazissis, P. Ring, Phys. Rev. C 69 (2004) 047301.
- [79] T. Niksic, D. Vretenar, P. Ring, Phys. Rev. C 78 (2008) 034318.
- [80] M. Kortelainen, J. McDonnell, W. Nazarewicz, P.-G. Reinhard, J. Sarich, N. Schunck, M. V. Stoitsov, S. M. Wild, Phys. Rev. C 85 (2012) 024304.
- [81] B. A. Brown, Phys. Rev. C 58 (1998) 220.
- [82] M. Kortelainen, J. McDonnell, W. Nazarewicz, E. Olsen, P.-G. Reinhard, J. Sarich, N. Schunck, S. M. Wild, D. Davesne, J. Erler, A. Pastore, Phys. Rev. C 89 (2014) 054314.
- [83] S. Brandt, Statistical and computational methods in data analysis, Springer-Verlag, New York, 1997.

- [84] J. Dobaczewski, W. Nazarewicz, P.-G. Reinhard, J. Phys. G 41 (2014) 074001.
- [85] M. Kortelainen, T. Lesinski, J. Moré, W. Nazarewicz, J. Sarich, et al., Phys. Rev. C 82 (2010) 024313.
- [86] T. Bürvenich, D. Madland, P.-G. Reinhard, Nucl. Phys. A 744 (2004) 92.
- [87] A. Tarantola, Inverse problem theory and methods for model parameter estimation, SIAM, Philadelphia, 2005.
- [88] P.-G. Reinhard, W. Nazarewicz, Phys. Rev. C 87 (2013) 014324.
- [89] P.-G. Reinhard, J. Piekarewicz, W. Nazarewicz, B. K. Agrawal, N. Paar, X. Roca-Maza, Phys. Rev. C 88 (2013) 034325.
- [90] C. Mahaux, P. F. Bortignon, R. A. Broglia, C. H. Dasso, Phys. Rep. 120 (1985) 1.
- [91] X. Roca-Maza, M. Brenna, G. Colò, M. Centelles, X. V. nas, B. Agrawal, N. Paar, D. Vretenar, J. Piekarewicz, Phys. Rev. C 88 (2013) 024316.
- [92] J. Erler, P. Klüpfel, P.-G. Reinhard, Phys. Rev. C 82 (2010) 044307.
- [93] J. Piekarewicz, B. K. Agrawal, G. Colò, W. Nazarewicz, N. Paar, P.-G. Reinhard, X. Roca-Maza, D. Vretenar, Phys. Rev. C 85 (2012) 041302.
- [94] J. Erler, P.-G. Reinhard, J. Phys. G 42 (2014) 034026.
- [95] T. Bürvenich, K. Rutz, M. Bender, P.-G. Reinhard, J. Maruhn, W. Greiner, Eur.Phys.J A 3 (1998) 139.
- [96] J. Erler, C. J. Horowitz, W. Nazarewicz, M. Rafalski, P.-G. Reinhard, Phys. Rev. C 87 (2013) 044320.
- [97] P. B. Demorest, T. Pennucci, S. M. Ransom, M. S. E. Roberts, J. W. T. Hessels, Nature (London) 467 (2010) 209.
- [98] J. P. Blaizot, D. Gogny, B. Grammaticos, Nucl. Phys. A 265 (1976) 315.
- [99] J. P. Blaizot, Phys. Rep. 64 (1980) 171.
- [100] P.-G. Reinhard, Nucl. Phys. A 649 (1999) 305c.
- [101] M. Brack, C. Guet, H.-B. Håkansson, Phys. Rep. 123 (1985) 275.
- [102] M. Wang, G. Audi, A. Wapstra, F. Kondev, M. MacCormick, X. Xu, B. Pfeiffer, Chinese Physics C 36 (12) (2012) 1603.
- [103] J. Péter, Eur. Phys. J. A 22 (2004) 271.
- [104] P.-G. Reinhard, H. Flocard, Nucl. Phys. A 584 (1995) 467.
- [105] A. Ekström, G. R. Jansen, K. A. Wendt, G. Hagen, T. Papenbrock, B. D. Carlsson, C. Forssén, M. Hjorth-Jensen, P. Navrátil, W. Nazarewicz, Phys. Rev. C 91 (2015) 051301.
- [106] E. N. E. van Dalen, C. Fuchs, A. Faessler, Eur. Phys. J. A 31 (2007) 29.
- [107] S.-Y. Chang, J. Carlson, V. R. Pandharipande, K. E. Schmidt, Phys. Rev. Lett. 91 (2003) 050401.
- [108] G. Astrakharchik, J. Boronat, J. Casulleras, S. Giorgini, Phys. Rev. Lett. 93 (2004) 200404.
- [109] J. Maruhn, P.-G. Reinhard, E. Suraud, Simple models of many-fermions systems, Springer, Berlin, 2010.
- [110] U. Post, E. Wust, U. Mosel, Nucl. Phys. A 437 (1985) 274.
- [111] L. Bennour, J. Libert, M. Meyer, P. Quentin, Nucl. Phys. A 465 (1987) 35.
- [112] T. Duguet, P. Bonche, P.-H. Heenen, J. Meyer, Phys. Rev. C 65 (2002) 014310.
- [113] K. J. Pototzky, J. Erler, P.-G. Reinhard, V. O. Nesterenko, Eur. Phys. J. A 46 (2010) 299.
- [114] M. Bender, J. Dobaczewski, J. Engel, W. Nazarewicz, Phys. Rev. C 65 (2002) 054322.
- [115] L.-G. Cao, G. Colo, H. Sagawa, P. Bortignon, L. Sciacchitano, Phys. Rev. C 80 (2009) 064304.
- [116] P. Vesely, J. Kvasil, V. O. Nesterenko, W. Kleinig, P.-G. Reinhard, V. Y. Ponomarev, Phys. Rev. C 80 (2009) 031302.
- [117] J. Fleckner, U. Mosel, P. Ring, H.-J. Mang, Nucl. Phys. A331 (1979) 288.
- [118] J. Dobaczewski, J. Dudek, Phys. Rev. C 52 (1995) 1827, erratum in Phys. Rev. C55, 3177 (1997).
- [119] J. Maruhn, P.-G. Reinhard, P. Stevenson, M. Strayer, Phys. Rev. C 74 (2006) 027601.
- [120] V. O. Nesterenko, J. Kvasil, P. Vesely, W. Kleinig, P.-G. Reinhard, V. Y. Ponomarev, J. Phys. G 37 (2010) 064034.
- [121] P. Bonche, S. E. Koonin, J. W. Negele, Phys. Rev. C 13 (1976) 1226.
- [122] K.-H. Kim, T. Otsuka, P. Bonche, J. Phys. G 23 (1997) 1267.
- [123] C. Simenel, P. Chomaz, Phys. Rev. C 68 (2003) 024302.
- [124] T. Nakatsukasa, K. Yabana, Phys. Rev. C 71 (2005) 024301.
- [125] J. Maruhn, M. Kimura, S. Schramm, P.-G. Reinhard, H. Horiuchi, A. Tohsaki, Phys. Rev. C 74 (2006) 044311.

- [126] A. S. Umar, V. E. Oberacker, Eur. Phys. J. A 39 (2009) 243.
- [127] V. E. Oberacker, A. S. Umar, J. A. Maruhn, P.-G. Reinhard, Phys. Rev. C 82 (2010) 034603.
- [128] A. S. Umar, V. E. Oberacker, C. J. Horowitz, P.-G. Reinhard, J. A. Maruhn, Phys. Rev. C 92 (2015) 025808.
- [129] B. Schuetrumpf, K. Iida, J. A. Maruhn, P.-G. Reinhard, Phys. Rev. C 90 (2014) 055802.
- [130] C. Simenel, Eur. Phys. J. A 48 (2012) 152.
- [131] J. A. Maruhn, P.-G. Reinhard, P. D. Stevenson, A. S. Umar, Comp. Phys. Comm. 185 (2014) 2195.
- [132] N. Loebl, J. Maruhn, P.-G. Reinhard, Phys. Rev. C 84 (2011) 034608.
- [133] E. P. Wigner, Phys. Rev. 40 (1932) 749.
- [134] M. Brack, R. K. Bhaduri, Semiclassical Physics, Addison-Wesley, Reading, 1997.
- [135] G. F. Bertsch, S. Das Gupta, Phys. Rep. 160 (1988) 190.
- [136] E. Suraud, P.-G. Reinhard, New J. Phys. 16 (2014) 063066.
- [137] E. Chabanat, P. Bonche, P. Haensel, J. Meyer, R. Schaeffer, Nucl. Phys. A 635 (1998) 231.
- [138] N. Loebl, A. S. Umar, J. Maruhn, P.-G. Reinhard, P. Stevenson, O. V. E., Phys. Rev. C 86 (2012) 024608.
- [139] S.-J. Lee, A. Umar, K. Davies, M. Strayer, P.-G. Reinhard, Phys. Lett. B 196 (1987) 419.
- [140] P.-G. Reinhard, A. Umar, K. Davies, M. Strayer, S.-J. Lee, Phys. Rev. C 37 (1988) 1026.